Editors' Suggestion

Wilson loop approach to fragile topology of split elementary band representations and topological crystalline insulators with time-reversal symmetry

Adrien Bouhon,[1,*] Annica M. Black-Schaffer,[1] and Robert-Jan Slager[2,3]
[1]*Department of Physics and Astronomy, Uppsala University, Box 516, SE-751 21 Uppsala, Sweden*
[2]*Max-Planck-Institut für Physik komplexer Systeme, 01187 Dresden, Germany*
[3]*Department of Physics, Harvard University, Cambridge, Massachusetts 02138, USA*

(Received 3 May 2018; revised manuscript received 4 October 2019; published 21 November 2019; corrected 10 February 2020)

We present a general methodology toward the systematic characterization of crystalline topological insulating phases with time-reversal symmetry. In particular, taking the two-dimensional spinful hexagonal lattice as a proof of principle, we study windings of Wilson loop spectra over cuts in the Brillouin zone that are dictated by the underlying lattice symmetries. Our approach finds a prominent use in elucidating and quantifying the recently proposed "topological quantum chemistry" concept. Namely, we prove that the split of an elementary band representation (EBR) by a band gap must lead to a topological phase. For this we first show that in addition to the Fu-Kane-Mele $\mathbb{Z}_2$ classification, there is $C_2\mathcal{T}$-symmetry-protected $\mathbb{Z}$ classification of two-band subspaces that is obstructed by the other crystalline symmetries, i.e., forbidding the trivial phase. This accounts for all nontrivial Wilson loop windings of split EBRs *that are independent of the parametrization of the flow of Wilson loops*. Then, by systematically embedding all combinatorial four-band phases into six-band phases, we find a refined topological feature of split EBRs. Namely, we show that while Wilson loop winding of split EBRs can unwind when embedded in higher-dimensional band space, two-band subspaces that remain separated by a band gap from the other bands conserve their Wilson loop winding, hence revealing that split EBRs are at least "stably trivial," i.e., necessarily nontrivial in the nonstable (few-band) limit but possibly trivial in the stable (many-band) limit. This clarifies the nature of *fragile* topology that has appeared very recently. We then argue that in the many-band limit, the stable Wilson loop winding is only determined by the Fu-Kane-Mele $\mathbb{Z}_2$ invariant implying that further stable topological phases must belong to the class of higher-order topological insulators.

DOI: 10.1103/PhysRevB.100.195135

I. INTRODUCTION

With the prediction and experimental verification of topological insulators [1–6], interest in band structures has been heavily reinvigorated over the past decade. In particular, it has been found that nontrivial topological structures may emerge due to the presence of symmetries leading to robust physical signatures such as helical edge states and defect modes [7–14], which have significantly extended the seminal founding of the quantum Hall effect (QHE). More recently, further interest has been focused on the interplay between topology and the underlying crystal symmetries, leading to the uncovering of an enriched landscape of topological phases [15–38]. These classification pursuits have revealed the existence of new invariants, effectively conveying obstructions to deform the band structure to a trivial insulating state in the atomic limit, and accordingly new types of edge and surface states. Still, it is of large practical and theoretical interest to understand these phases from a concrete perspective and consider their response to well-established probes. A prime example in this regard are Wilson loops [16,20,24–27,30,34,39–42].

In this work we study the relation between crystalline symmetries and the structure of Wilson loop spectra with the aim of using them as clear indicators of nontrivial topologies. In order to do so, we systematically account for all symmetries that span the little groups at high-symmetry points (HSP) of the Brillouin zone (BZ) and the compatibility relations between them. This is effectively done through the characterization of the band structures in terms of the irreducible representations (IRREPs) of the underlying space groups, which can be shown to match the descriptive equivariant K theory in the absence of spins and time-reversal symmetry (TRS) [31,32] and has been extended heuristically to the spinful case including TRS [35,43,44]. In particular, we derive the symmetry-protected windings of the Wilson loop spectra over patches of the BZ that have been chosen such as to take advantage of all available crystalline symmetries. In the process we map out the different topological sectors and also quantitatively evaluate whether insulating band structures, which split an elementary band representation [36,41,42,45–50] (EBR), must be topological. This general idea was postulated in Refs. [36,50] and lies at the core of the "topological quantum chemistry" (TQC) concept.

Preceding our work, Ref. [41] has rigorously related the topology of split EBRs with the symmetry-protected quantization of Wilson loop spectra over special base loops. Furthermore, Ref. [24] had early revealed the existence of a Wilson

*adrien.bouhon@physics.uu.se

loop winding in spinful topological insulators with inversion symmetry. An example of Wilson loop winding in a split spinless EBR has also been shown in Ref. [42], however, without a proof that it cannot be trivialized.

In this work we rigorously characterize the topology of split (spinful) EBRs in terms of an obstructed $\mathbb{Z}$ classification of the winding of Wilson loop spectra over the BZ combining the homotopy of the flow of two-band Wilson loops and the symmetry quantization of Wilson loops over special base loops. Furthermore, we reveal a refined topological feature of split EBRs under the addition of extra bands. Namely, we show that even when multiband Wilson loops can be unwinded, two-band subspaces that remain separated by a band gap from the other bands conserve their Wilson loop winding. This in particular allows us to elucidate the recently coined concept of "fragile topology" [51] from a quantitative as well as clear conceptual perspective. Finally, we argue that only the stable Fu-Kane-Mele $\mathbb{Z}_2$ invariant characterizes the winding of the Wilson loop in the many-band limit, implying that the further stable topological phases fall in the class of the higher-order topological insulators [52,53].

Altogether, this sets the basis toward a systematic classification of topological crystalline phases with TRS, where we rigorously position fragile topology of split EBRs as the bridge in crystalline systems between unstable topology, i.e., pertaining to few-band models (e.g., Hopf insulators), and stable topology, i.e., unaffected by the addition of trivial bands (e.g., Chern insulators).

To concretize the discussion, we consider the honeycomb lattice and focus on the specific symmorphic layer groups No. 80 (L80) and No. 77 (L77) [54,55]. For simplicity, we set one orbital per site. This nonetheless does not compromise the generality of our results as they illustrate an entirely generic and systematic method that can be extended to any other context as it reveals a direct relation between crystalline invariants and the flow of Wilson loop spectra over patches of the Brillouin zone that are dictated by the lattice symmetries. L80 contains inversion symmetry ($\mathcal{I}$) and is characterized by the point group D_{6h}, which incidentally also contains mirror symmetry with respect to the basal plane (σ_h). L77 on the contrary does not include inversion nor basal mirror symmetries and is characterized by the point group C_{6v}. For both layer groups, the honeycomb lattice corresponds to Wyckoff's position $2b$ such that the unit cell contains only two sublattice sites.[1] Later in the work we also consider the effect of coupling the honeycomb lattice with the triangular lattice made of the sublattice sites located at the center of the honeycombs, i.e., they realize the Wyckoff's position $1a$ of L80 and L77. We assume time-reversal symmetry (TRS) throughout the work.

Having set the stage, the work is organized in the following way. In Sec. II we derive the exhaustive classification of two-band spinless topological semimetallic phases for the honeycomb lattice. We show that on top of the well-known essential nodal point at K ("Dirac cone") characterized by a "π" Berry phase, an infinity of distinct topological phases exists corresponding to the accumulation of symmetry-protected nodal points which cannot be removed as long as the band gap remains open at the high-symmetry points (Γ, M). For this we use a global approach that goes beyond local ($\boldsymbol{k}\cdot\boldsymbol{p}$)-type analysis.

Once the spinless classification is known, we move on to answering the question of the effect of spin-orbit coupling (SOC). We start with the inversion-symmetric case for which SOC always gaps the spinless band structure. In Sec. III we derive the exhaustive classification of four-band spinful topological insulating phases for the honeycomb lattice when inversion symmetry is conserved. The classification of the spinful inversion-symmetric case is done in terms of the flow of the spin-polarized U(1) Berry phase (i.e., providing the spin-polarized Chern number). When the spin components cannot be separated, i.e., by breaking inversion symmetry, the classification must be done in terms of the flow of U(2) Wilson loop over the BZ. For this we introduce in Sec. IV the Wilson loop winding and relate it to the symmetry-protected quantization of Wilsonian phases over special base loops of the BZ. In particular, we show that while $C_{2z}\mathcal{T}$ symmetry (rotation combined with TRS) protects a $\mathbb{Z}$ Wilson loop winding for two-band subspaces, the C_3 symmetry of the hexagonal lattice acts as an obstruction that forbids the zero winding. As a consequence, a split EBR must be topologically nontrivial with a finite Wilson loop winding.

We then go further without inversion symmetry in Sec. V, where we show that the classification of spinful topological insulating phases with adiabatically broken inversion symmetry, i.e., for weak Rashba SOC, agrees with the classification with inversion symmetry. In particular, in this case the spinless classification can be lifted into the spinful context according to a one-to-two correspondence. When inversion symmetry is broken nonadiabatically, however, i.e., when Rashba SOC triggers a topological phase transition, the correspondence between the spinless and the spinful classifications is lost. We overcome this in Sec. VI where we present a mechanism based on the spin locking between Γ and K of a set of smooth, periodic, and rotation-symmetric Bloch functions that span the occupied subspace, i.e., a frame made out of sections of the vector bundle. Since this frame diagonalizes both the Wilson loop and the matrix representation of rotations, we obtain the symmetry-protected quantization of Wilson loop spectra and the constraints from symmetry on the set of allowed Wilson loop windings over the BZ. This leads to the quantitative characterization of the topology of split EBRs in terms of Wilson loop winding. Furthermore, our approach gives the quantitative as well as conceptual clarification of a new topological phase reported recently by Ref. [51], where it was called "fragile topology" after showing that it can be adiabatically mapped onto an atomic insulator (i.e., with a symmetric and localized Wannier representation) when extra trivial bands are included.

Given the finding of Ref. [51], a natural task is to determine the stability of the topology of split EBRs. For this, we study numerically in Sec. VII the six-band case by including an extra sublattice site at the center of the unit cells, i.e., coupling

[1] All the crystallographic and group-theoretic data can be found in the International Tables for Crystallography [54,55] and the Bilbao Crystallographic Server [57,73]. The tables of IRREPs used in the work were retrieved from the Bilbao Crystallographic Server using the space groups SG183 (L77), SG191 (L80), and SG175 (L75).

the honeycomb lattice (Wyckoff's position 2*b* of L77) with the triangular lattice (Wyckoff's position 1*a* of L77). We find that the Wilson loop windings of two-band subspaces that originate from a split EBR are unstable under the *nonadiabatic* coupling with extra trivial bands (i.e., closing the energy gap), and this independently of the set of IRREPs of the bands under consideration hence greatly generalizing the finding of Ref. [51]. Based on the results of Sec. VII, we give in Sec. VIII a detailed discussion for all the combinatorial ways of forming two- and four-band subspaces. We show that while the many-band Wilson loops loose the $\mathbb{Z}$-type winding breaking down to the $\mathbb{Z}_2$ Fu-Kane-Mele classification, the two-band subspaces originating from a split EBR that remain separated from the other bands by a band gap do conserve their nonzero Wilson loop winding. We argue that this fragile topology of split EBRs is related to the existence for two-band subspaces of a smooth (periodic) and rotation-symmetric Bloch frame over special base loops of the BZ, while such a frame fails to exist in four-band subspaces. This provides a rigorous characterization of the fragile topology of split EBRs within homotopy theory of vector bundles. Furthermore, we identify the patterns of Wilson loop spectra that survive as the number of bands is increased, thereby identifying the Fu-Kane-Mele $\mathbb{Z}_2$ invariant as the only invariant that characterizes the Wilson loop winding in the many-band limit. Our results thus bridge the gap between unstable topology, as described by homotopy theory for few-band models, and stable topology that is captured by K theory and is unchanged under the addition of trivial bands. We eventually briefly discuss the breaking of $C_{2z}\mathcal{T}$ and TRS from which insulating phases with a high Chern number can be generated.

Let us end this introduction with a note on terminologies. We follow for convenience the vocabulary of TQC given very recently in Refs. [36,50]. A band representation (BR) is any band structure in reciprocal space that is induced from a basis set of degrees of freedom localized in real space, i.e., represented by localized Wannier functions, such that the set is closed under all the symmetries of the system, i.e., each symmetry acts as a permutation of the Wannier functions. A BR is composite if it is equivalent to a direct sum of BRs. An EBR is a BR that is not composite. Whenever a BR also satisfies TRS is called a physical band representation (PBR). Therefore, in this work all the BRs are physical. A general band representation, or a quasiband representation (qBR), is any group of bands isolated from the other bands by an energy gap, i.e., it must satisfy all the compatibility relations that connect the IRREPs of the different regions of the BZ.

II. SPINLESS CASE

Let us start the discussion with the well-known characterization of nodal charges in spinless systems in terms of the Berry phase. A special feature of the spinless two-band model is that inversion symmetry ($\mathcal{I}$) and spinless TRS ($\mathcal{T}^2 = +1$) are both effectively satisfied. Hence, the results of this section characterize both Altland-Zirnbauer (AZ) classes [9] A and AI, and the two layer groups L77 and L80, i.e., AI + L80($2b$) $\cong$ A + L77($2b$) for a two-band model. While we refer to the symmetry class AI + L80($2b$) in this section, we use the fewer IRREPs of L77 for convenience. We give the relevant IRREPs for the little cogroups at Γ, K, and M in Table I.

TABLE I. Spinless IRREPs of rotations of the little cogroups [56] at Γ, K, and M, for the layer groups L77, L80, and L75. Retrieved from the Bilbao Crystallographic Server [57].

Γ	C_{6v}	D_{6h}	C_{6h}	C_{2z}	C_{3z}
	Γ_1	Γ_2^-	Γ_1^-	1	1
	Γ_4	Γ_3^+	Γ_2^+	-1	1
K	C_{3v}	D_{3h}	C_{3h}	C_{3z}	
	K_3	K_6	K_4	$e^{i2\pi/3}$	
			K_6	$e^{-i2\pi/3}$	
M	C_{2v}	D_{2h}	C_{2h}	C_{2z}	
	M_1	M_2^-	M_1^-	1	
	M_4	M_3^+	M_2^+	-1	

The EBR of the spinless honeycomb lattice is two dimensional as a result of the fact that the two sublattice sites are inseparable under L77, e.g., C_6 symmetry exchanges A and B sites. The two-band EBR is characterized by the IRREPs at the high-symmetry points (HSPs) and high-symmetry lines (HSLs) of the BZ according to Fig. 2(a). The simple nodal point (NP) at K is an essential degeneracy of AI + L80($2b$) such that the EBR cannot be split, i.e., no band gap can separate the two bands over the BZ. It follows that the system must be a topological semimetal at half-filling, i.e., there is one (spinless) electron per unit cell. In the following we always consider the half-filled case with a formal Fermi level set such that half of the eigenstates have energy below and half have energy above the Fermi level.

The stability of the NP is captured by the Berry phase computed over a base loop that encircles the NP and where only the occupied eigenstate is taken into account. Let us first consider the half-BZ (HBZ) patch S_α that is bounded by the oriented loop $l_\alpha \sim l_{MM}^{-1} \circ l_{\Gamma M}$ (blue solid line in Fig. 1, where $\sim$ means that we discard the two segments that cancel each other under a translation by a reciprocal lattice vector), where we write $l_{P_2P_1}$ an oriented open loop in momentum space that threads the BZ starting at P_1, crossing P_2, and ending at the shifted point $P_1 + \boldsymbol{K}$ ($P_{1,2} \in \{\Gamma, K_{1,2}, M_{1,2,3}\}$, $\boldsymbol{K} = \pm\boldsymbol{b}_{1(2)}$, see Fig. 1), and l^{-1} is the loop l in the reversed orientation. Folding [20,27,30,34] $l_{\Gamma M}$ and l_{MM} with C_{2z}, we find the Berry phase factor ($\gamma[l_\alpha] \equiv \gamma_\alpha$)

$$e^{i\gamma_\alpha} = \xi_2^\Gamma \left(\xi_2^M\right)^3, \tag{1}$$

where $\xi_n^{\bar{\boldsymbol{k}}}$ is the C_{nz} rotation symmetry eigenvalue of the occupied eigenstate at HSP $\bar{\boldsymbol{k}}$, i.e., given the allowed IRREPs of Fig. 2(a) these are $\xi_2^\Gamma = \xi_2^M = +1$ for the IRREPs Γ_1 and M_1, and $\xi_2^\Gamma = \xi_2^M = -1$ for the IRREPs Γ_4 and M_4. This leads to a $\mathbb{Z}_2$ quantization of the Berry phase. For instance, given the occupied IRREPs of Fig. 2(a) we find that the NP at K is characterized by a π Berry phase or, strictly speaking, by the set $\gamma_\alpha \in \{\pi + n2\pi\}_{n\in\mathbb{Z}}$ which we write as a congruence relation $\gamma_\alpha = \pi \pmod{2\pi}$. Performing a band inversion at Γ, $\Gamma_4 \leftrightarrow \Gamma_1$ (or similarly at M, $M_1 \leftrightarrow M_4$) an extra simple NP must appear on each HSL $\Lambda \equiv \overline{\Gamma K}$ (respectively $T \equiv \overline{MK}$). Indeed, band crossings over Λ (T) cannot be avoided due to

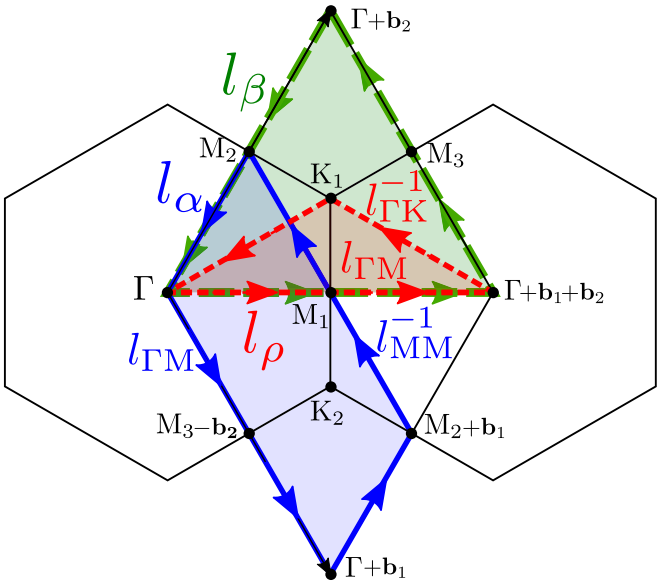

FIG. 1. First BZ of the honeycomb lattice spanned by the primitive reciprocal vectors $\boldsymbol{b}_1$ and $\boldsymbol{b}_2$. High-symmetry points (HSP) Γ, K, and M. Inequivalent high-symmetry points are written with different subscripts, i.e., K_1, K_2, M_1, M_2, M_3. Half Brillouin zone (HBZ) patches S_α (blue) and S_β (green), with their respective oriented boundaries $l_\alpha \sim l_{MM}^{-1} \circ l_{\Gamma M}$ (blue) and l_β (dashed green), and the patch S_ρ (red) bounded by $l_\rho = l_{\Gamma K}^{-1} \circ l_{\Gamma M}$ (dotted red) covering one sixth of the BZ. $l_{P_2P_1}$ is the oriented open loop that threads the BZ starting at point P_1, crossing P_2 and ending at the shifted point $P_1 + \boldsymbol{K}$ with the reciprocal lattice vector $\boldsymbol{K} = \pm\boldsymbol{b}_{1(2)}$. We mean by $\sim$ equal up to segments that cancel each other through a translation by a reciprocal lattice vector. Note that the different segments of the curves directly correspond to the underlying crystal symmetries.

the distinct symmetry characters of the bands with respect to the vertical mirror symmetries of the HSL as marked by the IRREPs $\Lambda_{1,2}$ and $T_{1,2}$ [see Fig. 2(a)]. We now have four simple NPs within the HBZ S_α, but Eq. (1) gives $\gamma_\alpha = 0 \,(\mathrm{mod}\, 2\pi)$ such that this C_{2z}-based computation of the Berry phase loses track of the NPs.

In order to have a finer definition of the Berry phase which takes advantage also of the other crystalline symmetries, let us now consider the HBZ patch S_β bounded by the oriented loop l_β (green dashed line in Fig. 1). Contrary to l_α, l_β exhibits the C_{3z} symmetry of the K point which allows us to split it into three symmetric sections. A third of the loop can therefore be taken as the path beginning at M_2 crossing Γ and ending at M_1, i.e., $l'_\beta = l_{M_1\Gamma} \circ l_{\Gamma M_2}$. Then, using a smooth reference gauge for the eigenstates, we find the noncyclic Berry phase over the loop segment l'_β (see derivation in Appendix A 4)

$$e^{i\gamma'_\beta} = \frac{2 - (1 + i\sqrt{3})\xi_2^\Gamma \xi_2^M}{2 - (1 - i\sqrt{3})\xi_2^\Gamma \xi_2^M}, \tag{2}$$

with the symmetry eigenvalues of the occupied eigenstate determined by

$$\begin{aligned} \xi_2^\Gamma &= -\mathrm{sign}\{\mathrm{Re}[h_{AB}(\Gamma)]\}, \\ \xi_2^M &= \mathrm{sign}\{\mathrm{Re}[h_{AB}(M)]\}. \end{aligned} \tag{3}$$

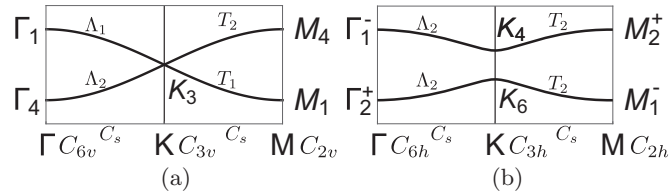

FIG. 2. Examples of band structures for the EBRs of (a) spinless symmetry class A + L77($2b$) $\cong$ AI + L80($2b$), and (b) spinless symmetry class A + L75($2b$), when restricted to Wyckoff's position $2b$. Notations from the Bilbao Crystallographic Server [57] for the IRREPs of the space groups.

Here, $h_{AB}(\boldsymbol{k})$ is the off-diagonal element of the tight-binding model written in the Bloch basis $\sum_{\boldsymbol{R}_n} e^{i\boldsymbol{k}(\boldsymbol{R}_n + \boldsymbol{r}_{A(B)})} |w_{A(B)}, \boldsymbol{R}_n\rangle$ where $\boldsymbol{R}_n$ labels the unit cells, $\boldsymbol{r}_{A(B)}$ is the sublattice position within one unit cell, and $\langle \boldsymbol{r}|w_{A(B)}, \boldsymbol{R}_n\rangle = w(\boldsymbol{r} - \boldsymbol{R}_n - \boldsymbol{r}_{A(B)})$ gives a complete basis set of localized Wannier functions (see Appendix A 1 for more details). Therefore, since by rotational symmetry $e^{i\gamma_\beta} = (e^{i\gamma'_\beta})^3$, we find for the phase winding over the entire loop l_β

$$\gamma_\beta = \begin{cases} \pi \,(\mathrm{mod}\, 6\pi) & \text{if } \xi_2^\Gamma \xi_2^M = -1, \\ -2\pi \,(\mathrm{mod}\, 6\pi) & \text{if } \xi_2^\Gamma \xi_2^M = +1. \end{cases} \tag{4}$$

from which we define the winding number $W_I = \gamma_\beta/\pi$.

W_I is the topological invariant that classifies all symmetry-protected topological semimetallic phases of the spinless graphene model with a single orbital per site. We illustrated this with the numerical examples of Fig. 3 that realize $W_I = +1$, -2, $+4$, and -5. For each case, we show the band structure, the noncyclic Berry phase over the loop segment l'_β, and the schematic configuration of NPs within the HBZ patch S_β. Starting from a band structure with a single NP at K for which $W_I = +1$ shown in Fig. 3(a), the other topological sectors are reached through successive band inversions at Γ and M triggered by tight-binding parameters of increasing range.[2] For instance, restricting the tight-binding model to the nearest-neighbor parameters, only the single NP at K can be formed, while we included up to the seventh layer of neighbors in order to generate the higher winding of Fig. 3(d). Each band inversion leads to a jump of the winding number by ± 3, as predicted by Eq. (4). We conclude that the two-band model of the honeycomb lattice at half-filling is classified by

$$\pi_1^{(l_\beta)}\left(\mathcal{H}^{1+1}_{\mathrm{AI+L80}(2b)}\right) \cong \mathbf{1} + 3\mathbb{Z} \quad \ni \quad W_I = \frac{\gamma_\beta}{\pi}, \tag{5}$$

where $\pi_1^{(l_\beta)}$ means the first homotopy group restricted to the C_3-symmetric base loops l_β connecting Γ and the three inequivalent M points, $\mathcal{H}^{1+1}_{\mathrm{AI+L80}(2b)}$ is the classifying space (Grassmannian) of the two-band Hamiltonian at half-filling (1 occupied state + 1 unoccupied state) for the symmetry class

[2]We also find a topological transition with no band inversion at Γ or M happening through the closing of a whole nodal line encircling Γ (or similarly three nodal lines encircling the M points). However, such a nodal line is realized only at fine-tuned values of the microscopic parameters.

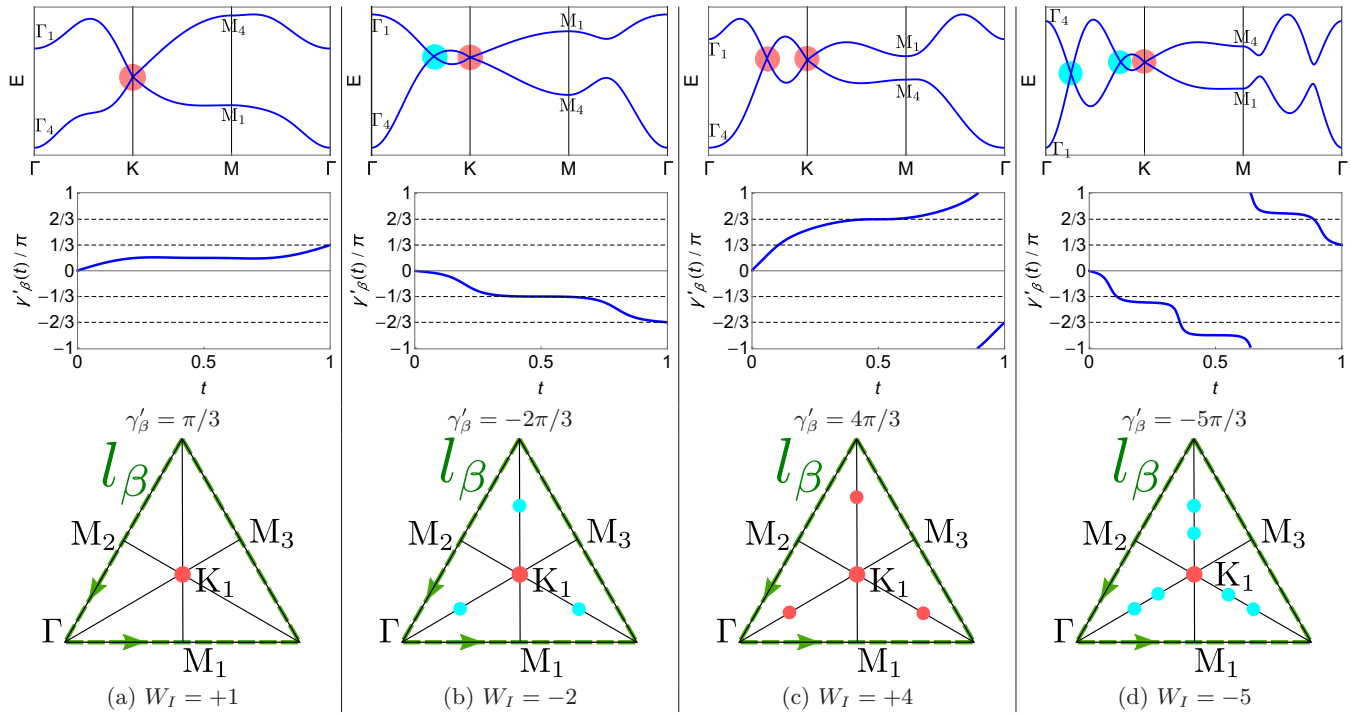

FIG. 3. Spinless topological semimetallic phases of the honeycomb lattice reached through band inversions at Γ and M triggered by tight-binding parameters of increasing range. Columns (a)–(d) correspond to an increasing number of simple nodal points protected by crystalline symmetries. First row: band structures along the high-symmetry lines of the BZ. Second row: noncyclic Berry phase along one third of the C_3-symmetric loop l_β encircling K. Third row: schematic configuration of symmetry-protected nodal points within the HBZ S_β bounded by l_β (nodal points in red have $W_I = +1$, and in blue $W_I = -1$). Crystalline winding numbers are (a) $W_I = \gamma_\beta/\pi = +1$, (b) $W_I = -2$, (c) $W_I = +4$, and (d) $W_I = -5$.

AI + L80(2b). The offset **1** marks the obstruction due to the essential NP at K that forbids the trivial phase.

It is important to note that the topological content of Eqs. (4) and (5) is *relative* and not *absolute* [58]. This means that they hold under the following relative assumptions. (i) A reference trivialization of the total Bloch bundle has been fixed. Practically this is done through the choice of a complete basis set of Bloch functions, here obtained from a complete basis set of localized Wannier functions [59]. (ii) The eigenstates are defined within the same smooth reference gauge. This is done in the Appendix through the choice of the global analytical ansatz for the wave function (see also the discussion on gauge transformation in Appendix A 5). (iii) Large gauge transformations are excluded.[3] (iv) The HSP K_1 has been chosen as a representative (choosing K_2 instead, while keeping fixed the origin of the Bravais lattice, reverses the winding numbers with the offset $-\mathbf{1}$). We also note that for a given winding number W_I of the occupied subspace we find the reversed winding $-W_I$ for the unoccupied subspace. It is also worth noting that our approach is global in the sense that the results (4) and (5) are derived from a wave function that is smooth over the whole BZ (discarding the singularities at the NPs)[4] (see the details in Appendix A 2), hence allowing us to go significantly beyond the local $\boldsymbol{k}\cdot\boldsymbol{p}$ approach [60].

Finally, we note that the $\mathbb{Z}$-type structure of Eq. (5) can be understood as inherited from the few-band result $\pi_1(\mathcal{H}^{1+1}_{\mathrm{AI}+\mathcal{I}}) = \mathbb{Z}$ [61]. In our case, the crystalline symmetries act as an obstruction within the classifying superspace $\mathcal{H}^{1+1}_{\mathrm{AI}+\mathcal{I}}$ such that only a subset of the topological sectors are allowed ($\mathbf{1} + 3\mathbb{Z} \subset \mathbb{Z}$) excluding the trivial phase. In general, for a two-dimensional spinless system (or a two-dimensional momentum subspace) with no inversion symmetry, we can instead use the symmetry class AI + $C_{2\perp}\mathcal{T}$ (with the $C_{2\perp}$ axis perpendicular to the system, here C_{2z}) since $C_{2\perp}\mathcal{T}$ similarly imposes a reality condition on the classifying space within the σ_h mirror invariant plane ($\sigma_h = C_{2\perp}\mathcal{I}$) leading again to $\pi_1(\mathcal{H}^{1+1}_{\mathrm{AI}+C_{2\perp}\mathcal{T}}) = \mathbb{Z}$ [62,63].

III. SPINFUL CASE WITH INVERSION SYMMETRY

Having shown that the noncyclic Berry phase is able to characterize the extra structure from the impact of crystalline symmetries in the case of spinless semimetallic phases, we now move to the spinful AZ symmetry class AII that is relevant when SOC is turned on [9]. Due to the spin degree of freedom, the Hamiltonian is now 4×4 and we concentrate on the fully gapped phase at half-filling.

[3] While large gauge transformations are allowed within equivalence classes defined up to bundle isomorphisms, they carry their own nontrivial windings and hence permit to jump between different homotopy equivalence classes (see Ref. [58]).

[4] A global smooth gauge is allowed by the vanishing of the first Chern class in the gapless phase [90].

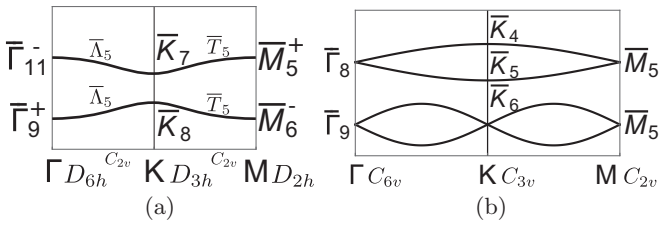

FIG. 4. EBRs for (a) spinful symmetry class AII + L80($2b$) and (b) spinful symmetry class AII + L77($2b$), when restricted to the Wyckoff's position $2b$. Notations from the Bilbao Crystallographic Server [57] for the IRREPs of the space groups.

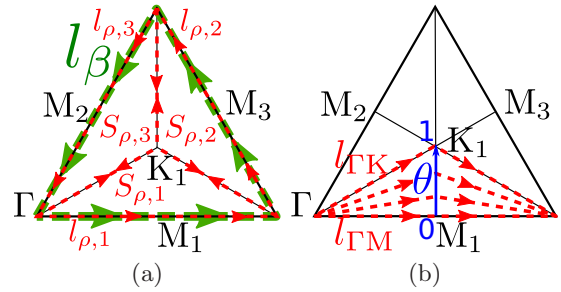

FIG. 5. (a) Symmetry decomposition of the HBZ patch $S_\beta = S_{\rho,1} + S_{\rho,2} + S_{\rho,3}$ bounded by $l_\beta \sim l_{\rho,3} \circ l_{\rho,2} \circ l_{\rho,1}$. (b) Loop parametrization of the patch $S_\rho = \bigcup_{\theta\in[0,1]} l_\theta$ with $l_0 = l_{\Gamma M}$ and $l_1 = l_{\Gamma K}$.

In this section we focus on the case with inversion symmetry, i.e., we characterize the topology of the symmetry class AII + L80($2b$). Basal mirror symmetry ($\sigma_h = C_{2z}\mathcal{I}$) forbids spin-flip terms in the four-band Hamiltonian such that it can be separated into spin-up and -down sectors leading to the decomposition $\mathcal{H}^{2+2}_{\text{AII+L80}(2b)} = \mathcal{H}^{1+1}_{\uparrow} \oplus \mathcal{H}^{1+1}_{\downarrow}$ which makes the expectation value of the z-spin component s_z a good quantum number over the whole BZ. Practically, the generic tight-binding Hamiltonian of this symmetry class corresponds to a generalized Kane-Mele model, i.e., including arbitrary many neighbors, with zero Rashba SOC and no staggered potential (as to preserve inversion and C_{2z} symmetry).

A direct consequence of the spin separation is that the topological classification is reduced to that one of the spin-polarized subspaces. Let us address the spinless symmetries of each spin-polarized subspace, i.e., when we forget about the spin. Contrary to the spinless case (AI + L80), the spin-polarized subspaces $\mathcal{H}^{1+1}_{\sigma}$ have no spinless TRS, i.e., the AZ symmetry class is lowered as AI → A, nor spinless vertical mirror symmetries, i.e., the lattice symmetry class is lowered as L80(D_{6h}) → L75(C_{6h}) which is effectively similar to the effect of an external magnetic field perpendicular to the basal plane. As a consequence, the spin-polarized subspaces have no essential degeneracy at K (see Appendix B for details) and the band structure at half-filling is fully gapped [see Fig. 2(b) showing the EBR of one spin subspace and Fig. 4(a) showing the EBR of the parent spinful class].

It follows that the topology of each gapped spin-polarized subspace can be characterized by a Chern number, or equivalently by the flow of Berry phase over the BZ [64]. We write this as $2\pi C_1[\text{BZ}] = \gamma[\partial\text{BZ}] - \gamma[\partial\mathbf{0}] = \gamma[\partial\text{BZ}]$ where ∂BZ is an oriented boundary of the BZ. Since the BZ is a closed manifold, ∂BZ is equivalent to a point and in the previous expression we assume that we have kept track of the Berry phase as we deform the base point $\partial\mathbf{0}$ into a loop that we then sweep over the whole BZ into ∂BZ, that is (topologically) a point again. It then follows that $\gamma[\partial\text{BZ}] = n2\pi$ (as a phase is defined modulo 2π) and the Chern number is given by the integer $n \in \mathbb{Z}$.

We now take advantage of the C_6 symmetry of the system and compute the Berry phase winding over the patch S_ρ that is one sixth of the whole BZ (a similar construction has already been used in Ref. [41] giving the constraint due to C_6 symmetry on the Chern number of a single isolated band). S_ρ is bounded by the oriented loop $l_\rho = l^{-1}_{\Gamma K} \circ l_{\Gamma M}$ (see Fig. 1), and by folding $l_{\Gamma M}$ with C_{2z} and $l_{\Gamma K}$ with C_{3z} we find (see the algebraic derivation using Wilson loop techniques in Appendix B 2)

$$e^{i\gamma_\rho} = \xi_2^\Gamma \xi_3^K \left(\xi_2^M \xi_3^\Gamma\right)^{-1} = \pm e^{\pm i\pi/3} \tag{6}$$

or $\gamma_\rho = \pm\pi/3 \,(\text{mod}\,\pi)$, where all possible permutations of the IRREPs composing the EBR [Fig. 2(b) and see also Table I] have been taken into account. This result is consistent with Ref. [41] with the difference that we also included the phases with a trivial Fu-Kane-Mele index (see below). Phase transitions between distinct topological sectors can be engineered through band inversions at Γ, K, and M triggered by tight-binding parameters of increasing range. Since all σ_h-symmetric SOC terms vanish at Γ and M the energy ordering of the IRREPs at these points is still determined by Eq. (3), while the IRREP of the occupied eigenstate at K is now dictated by $\text{sign}\{h_{AA,\sigma}(K) - h_{BB,\sigma}(K)\}$ (see Appendix B).

Combining the images of S_ρ under successive rotations by C_{3z} we recover the HBZ patch S_β introduced in the previous section, i.e., $S_\beta = S_{\rho,1} + S_{\rho,2} + S_{\rho,3}$ as shown in Fig. 5(a) with the boundary $l_\beta \sim l_{\rho,3} \circ l_{\rho,2} \circ l_{\rho,1}$ where $l_{\rho,2} \sim C_{3z} l_{\rho,1}$ and $l_{\rho,3} \sim C^2_{3z} l_{\rho,1}$ ($\sim$ here means equal up to a translation by a reciprocal lattice vector). The symmetry of the Berry curvature under C_{3z} rotation gives $e^{i\gamma_\beta} = (e^{i\gamma_\rho})^3$ and we conclude

$$\pi_2\left(\mathcal{H}^{2+2}_{\text{AII+L80}(2b)}\right) \cong \pm\mathbf{1} + 3\mathbb{Z} \ni W^{\mathcal{I}}_{II} = \frac{\gamma_\beta}{\pi}, \tag{7}$$

where the second homotopy group π_2 refers to the continuous maps from the whole BZ to the classifying space $\mathcal{H}^{2+2}_{\text{AII+L80}(2b)}$ with the approximation $\text{BZ} \cong \mathbb{T}^2 \to \mathbb{S}^2$. Therefore, the winding number $W^{\mathcal{I}}_{II}$ classifies all symmetry-protected topological insulating phases of the honeycomb lattice with SOC and inversion symmetry for a single orbital per site at Wyckoff's position $2b$. For instance, the Fu-Kane-Mele $\mathbb{Z}_2$ invariant is readily obtained as the parity $\nu_{\text{FKM}} = W^{\mathcal{I}}_{II} \bmod 2$. Concretely, the value of the winding number depends on the (spinless) IRREPs of the spin-polarized occupied eigenstate according to Eq. (6) and the winding increases with an increasing range of the tight-binding parameters. In particular, we can switch the sign of the winding number by switching the sign of $\{h_{AA,\sigma}(K) - h_{BB,\sigma}(K)\}$ that is nonzero only with SOC. Reintroducing the spin degrees of freedom, we have $\xi^{\bar{k}}_{2,\downarrow} = (\xi^{\bar{k}}_{2,\uparrow})^*$ and $\xi^{\bar{k}}_{3,\downarrow} = (\xi^{\bar{k}}_{3,\uparrow})^*$ from which follows $\gamma_{\rho,\downarrow} = -\gamma_{\rho,\uparrow}$ and $W^{\mathcal{I}}_{II,\downarrow} = -W^{\mathcal{I}}_{II,\uparrow}$. Similarly to Eq. (5), the classification of Eq. (7) has been derived under the assumption

that large gauge transformations are discarded, however, the explicit use of a smooth reference gauge is not needed in the algebraic computation of Appendix B 2. Nevertheless, Eq. (6) should still be interpreted in a relative sense, i.e., it gives the actual quantity obtained from the surface integral of the Berry connection derived from a smooth reference gauge over the patch S_ρ. Using the analytical ansatz of the spin-polarized eigenstate given in Appendix B we have verified numerically that both computations give the same results.

Importantly, we conclude from Eq. (7) that the classification of the spinless system (5) is lifted into the classification of inversion-symmetric spinful gapped phases with a doubling that is due to the spin grading, i.e., $W_I \in \mathbf{1}+3\mathbb{Z} \to W_{II}^{\mathcal{I}} \in \{\mathbf{1}+3\mathbb{Z}, -\mathbf{1}+3\mathbb{Z}\}$. We stress that the band structure is now gapped and that the winding number $W_{II}^{\mathcal{I}}$ captures a flow of Berry phase over the BZ, which then gives the Chern number of the two-dimensional gapped phase. Therefore, even though the form of Eq. (7) closely resembles Eq. (5) of the gapless phase, the interpretation of the winding number is different. It is also important to note that $W_{II}^{\mathcal{I}} = +1+3n$ and $W_{II}^{\mathcal{I}} = -1-3n$ do refer to two distinct topological classes in our classification. For instance, a reversal of $W_{II}^{\mathcal{I}}$ happens when the bands K_4 and K_6 are inverted in Fig. 2(b) that requires a closing of the band gap and thus constitutes a topological phase transition.

We note that the $\mathbb{Z}$-type classification is robust in the many-band case. This is the case when the system is symmetric under C_2 spin rotation along the z axis guaranteeing the separation of the spin sectors and leading to a classification of the topology in terms of the spin Chern number [22,65]. A more physical symmetry, however, is the basal mirror which also leads to a $\mathbb{Z}$ classification in the many-band case [22,66]. We here readily obtain the (spinful) mirror Chern number as $C_1^+ = 2W_{II}^{\mathcal{I}}\pi/(2\pi) = W_{II}^{\mathcal{I}} = \pm 1 \bmod 3$ for the even-mirror subspace, and $C_1^- = -C_1^+$ for the odd-mirror subspace. It is the special case of the 4×4 Hamiltonian with AII + L80 symmetry that the spin Chern number here matches with the mirror Chern number, i.e., there are not enough bands to break the spin-rotation symmetry without breaking the symmetries of L80.

IV. WILSON LOOP WINDING

Breaking inversion (equivalently basal mirror) symmetry allows spin-flip Rashba SOC terms that forbid the spin decomposition of Sec. III. Nevertheless, the topological classification must be preserved when inversion symmetry is broken adiabatically, i.e., without closing the band gap [67]. However the question remains of a direct verification that goes beyond the previous derivation of the Berry phase based on s_z being a good quantum number over the whole BZ. Because of the spin grading, we must switch from a U(1) Berry phase to a U(2) Wilson loop [16,20,24–27,39] description of the two-band occupied subspace.[5]

In this section we first review known properties of the Wilson loop that follow from TRS and $C_{2z}\mathcal{T}$ symmetry [25], from which we motivate the existence of nontrivial windings of the Wilson loop over the BZ. Wilson loop winding has been used in a gauge-invariant computation of the Fu-Kane-Mele $\mathbb{Z}_2$ invariant [39]. It has also been shown to capture a crystalline invariant of systems with inversion symmetry [24], and Ref. [42] has recently shown one example of a spinless Wilson loop winding protected by C_2 symmetry. We derive here the expression of the spinful Wilson loop winding over one patch of the BZ that captures the effect of crystalline symmetries, i.e., here the point group D_{6h} or C_{6h}. The Wilson loop characterization of the topological sectors will then allow us to treat the cases when s_z is not a good quantum number leading to a complete classification of the symmetry class AII + L77(2b), i.e., including the inversion-symmetry-breaking topological phases that are not adiabatically connected to the phases classified by Eq. (7).

Let us first introduce some notations. We write the Wilson loop computed over a momentum base loop l as $\mathcal{W}_l \equiv \mathcal{W}[l]$. The Wilson loop spectrum is gauge invariant due to the invariance of the eigenvalues under unitary transformations. Writing it as $\mathrm{eig}\{\mathcal{W}_l\} = [e^{i\varphi_{l,1}}, e^{i\varphi_{l,2}}]$, this defines the Wilsonian phases $\varphi_{l,1}$ and $\varphi_{l,2}$.

Whenever a loop satisfies the symmetry $\mathcal{I}l = l^{-1}$, we have $\mathcal{W}_{\mathcal{I}l} = \mathcal{W}_l^{-1}$ and spinful TRS ($\mathcal{T}^2 = -1$) gives $A\mathcal{W}_l^* A^{-1} = \mathcal{W}_{\mathcal{I}l} = \mathcal{W}_l^{-1}$ where $A\mathcal{K}$ is the antiunitary representation of TRS in the occupied band basis (A is unitary and $\mathcal{K}$ is the complex conjugation) and $(A\mathcal{K})^2 = -\mathbb{I}$. Such base loops must connect time-reversal-invariant momenta (TRIMPs) leading to a Wilson loop spectrum that is composed of Kramers pairs, i.e., pairs of mutually orthogonal eigenstates with the same Wilsonian eigenvalue [25]. This is true for the loops $l_{\Gamma M}$ and l_{MM} (Fig. 1). A formulation of the Fu-Kane-Mele $\mathbb{Z}_2$ invariant [2,7] then follows from the spectral flow of Wilson loop over the HBZ patch S_α bounded by $l_{MM}^{-1} \circ l_{\Gamma M}$ [39]. We note that the edges $l_{\Gamma M_2}$ and $l^{-1}_{\Gamma-\boldsymbol{b}_1, M_2-\boldsymbol{b}_1}$ of l_α can be neglected when large gauge transformations are excluded. Practically this is done by imposing the periodic gauge (see Appendix A 1). Also, the HBZ patch must be chosen such that the composition of the oriented boundary (e.g., l_α for S_α) with its image under inversion ($\mathcal{I}l_\alpha$) gives an oriented boundary of the whole BZ, i.e., $l_\alpha \circ \mathcal{I}l_\alpha \cong \partial\,\mathrm{BZ}$.

Considering now the combined symmetry $C_{2z}\mathcal{T} = \sigma_h\mathcal{K}$, the Wilson loop satisfies $U_{\sigma_h}\mathcal{W}_l^* U_{\sigma_h}^\dagger = \mathcal{W}_l$ where $U_{\sigma_h}\mathcal{K}$ is the antiunitary representation of $\sigma_h\mathcal{K}$ in the occupied band basis [25]. It follows that the eigenstates of the Wilson loop are composed of mutually orthogonal pairs with their eigenvalues being partners under complex conjugation, i.e., $\mathrm{eig}\{\mathcal{W}_l\} = [e^{i\varphi_l}, e^{-i\varphi_l}]$.[6] This feature has an important consequence for the topological classification of the flows of Wilson loop over the BZ. In order to see this, let us parametrize the BZ through loop sections as $\bigcup_{\theta\in\mathbb{S}^1} l_\theta \cong \mathbb{S}^1\times\mathbb{S}^1 \cong \mathbb{T}^2$ as follows naturally from the parametrization of the 2-torus $\mathbb{T}^2$

[5]The U(2) Berry-Wilczek-Zee connection matrix is defined as $\mathcal{A}_\mu^{mn} = \langle u_m, \boldsymbol{k}|\partial_{k^\mu} u_n, \boldsymbol{k}\rangle$ with $|u_n, \boldsymbol{k}\rangle$ the nth occupied cell-periodic Bloch eigenstate and the Wilson loop over a base loop l is given as $\mathcal{W}[l] = \exp\{-\oint_l d\boldsymbol{k}\cdot\boldsymbol{\mathcal{A}}(\boldsymbol{k})\}$.

[6]If V_l is an eigenvector of $\mathcal{W}_l$ with the Wilsonian eigenvalue $e^{i\varphi_l}$, then $U_{\sigma_h}^T V_l^*$ is also an eigenvector with the Wilsonian eigenvalue $e^{-i\varphi_l}$.

by two circles $\mathbb{S}^1$, where each θ labels one loop $l_\theta \cong \mathbb{S}^1$ of the BZ. By choosing one *representative* Wilsonian phase $\varphi(\theta)$, we can then classify the spectral flow of Wilson loop from the parameter base space $\mathbb{S}^1 \ni \theta$ into the classifying space $\mathrm{U}(1) \ni e^{i\varphi(\theta)}$ by a winding number since $\pi_1(\mathrm{U}(1)) = \mathbb{Z}$ [indeed, $\mathrm{eig}\{\mathcal{W}_l\} \in \mathrm{SO}(2) \cong \mathrm{U}(1)$]. Note here that the choice of $\varphi(\theta)$ instead of $-\varphi(\theta)$ is arbitrary.[7]

An important consequence of $C_{2z}\mathcal{T}$ symmetry is the double degeneracy of 0 and $\pm\pi$ Wilsonian phases. Another important feature that comes from the combined constraints of TRS and $C_{2z}\mathcal{T}$ symmetry is that for any loop connecting two TRIMPs and satisfying $l^{-1} = \mathcal{I}l$, the Wilson loop spectrum must be both doubly degenerated and symmetric under complex conjugation. Therefore, the two-band Wilson loop spectrum over $l_{\Gamma M}$ and l_{MM} must either be $[+1, +1]$ or $[-1, -1]$. It is worth noting that while we expect the $\mathbb{Z}$-type Wilson loop winding to be present in two-band subspaces with TRS and $C_{2z}\mathcal{T}$ symmetry, we do not expect that it is robust in subspaces with more bands. Indeed, the homotopy classification of flows of Wilson loop over the BZ, i.e., $\mathrm{eig}\{\mathcal{W}_{l_\theta}\} \in \mathrm{SO}(2n)$ with $\theta \in \mathbb{S}^1$, for $n > 1$ gives $\pi_1(\mathrm{SO}(2n)) = \mathbb{Z}_2$ [61]. This is confirmed in Secs. VII and VIII where we analyze six-band models and find a fragile topology of split EBRs.

Let us now consider the effect of the other crystalline symmetries. This is again revealed by considering the patch S_ρ bounded by $l_\rho = l_{\Gamma K}^{-1} \circ l_{\Gamma M}$ (Fig. 1). Similarly to the above parametrization of the whole BZ, we parametrize the patch S_ρ through loop sections as $l_\theta : [0, 1] \to S_\rho : \theta \mapsto l_\theta$ with $l_0 = l_{\Gamma M}$ and $l_1 = l_{\Gamma K}$ [see Fig. 5(b)]. Therefore, for each loop l_θ we can define a representative Wilsonian phase $\varphi(\theta) = \varphi[l_\theta]$ such that the winding of the Wilson loop is captured by the winding of $\varphi(\theta)$ over the patch S_ρ, i.e.,

$$\begin{aligned} W[S_\rho] &= \int_0^1 \frac{d\theta}{\pi}\frac{d\varphi(\theta)}{d\theta} \in \frac{1}{\pi}[\overline{\varphi}(1) - \overline{\varphi}(0)](\mathrm{mod}\,2), \\ \overline{\varphi}(0) &= \varphi(0) \in [-\pi, \pi), \\ \overline{\varphi}(1) &= (\varphi(1)\,\mathrm{modulo}\,2\pi) \in [-\pi, \pi), \end{aligned} \tag{8}$$

with $\varphi(0) = \varphi[l_{\Gamma M}]$ and $\varphi(1) = \varphi[l_{\Gamma K}]$, and where we have defined reference Wilsonian phases $\overline{\varphi}(0)$ and $\overline{\varphi}(1)$ with respect to which we compute the winding of the Wilson loop and where "modulo" here refers to the operation of taking the remainder as opposed to "mod" used to define a set.[8] Similarly to the computation of the Fu-Kane-Mele $\mathbb{Z}_2$ invariant from the spectral flow of the Wilson loop [39], TRS makes it sufficient to consider the Wilsonian flow over one HBZ. From the decomposition of the HBZ S_β into S_ρ patches as shown in Fig. 5(a), we find that the Wilson loop winding over S_β is given as $W[S_\beta] = 3W[S_\rho]$. Now, by conservation of the total flow over the BZ, the flow over the HBZ patch S_α must match with the flow over the HBZ patch S_β (note also that, as for the HBZ patch S_α, $\mathcal{I}l_\beta \circ l_\beta \cong \partial\mathrm{BZ}$) and we define the Wilson loop winding number

$$W_{II} \equiv 3W[S_\rho] = W[S_\beta] = W[S_\alpha]. \tag{9}$$

The Fu-Kane-Mele $\mathbb{Z}_2$ invariant is then obtained by taking the parity of this winding number, i.e., $\nu_{\mathrm{FKM}} = W_{II} \mod 2$.

We importantly note that the Wilson loop winding is supported by the homotopy of the flow of Wilson loop protected by $C_2\mathcal{T}$ symmetry [$\pi_1(\mathrm{SO}(2)) = \mathbb{Z}$]. It follows that while we use special cuts of the BZ to derive the constraints from crystalline symmetries on the Wilson loop, *the total Wilson loop winding (protected by $C_2\mathcal{T}$ symmetry) is independent of the parametrization of the flow over the BZ*, as shown explicitly in Fig. 6.

V. SPINFUL CASE WITH ADIABATIC BREAKING OF INVERSION SYMMETRY

We are now ready to address in detail the spinful case where inversion symmetry is only broken adiabatically. Inversion symmetry together with C_{2z} gives the basal mirror symmetry σ_h that makes s_z a good quantum number over the whole BZ, as we have seen in Sec. III. It then follows that with σ_h symmetry the Wilson loop spectrum takes the form $\mathrm{eig}\{\mathcal{W}_l\} = [e^{i\gamma_{l,\uparrow}}, e^{i\gamma_{l,\downarrow}}] = [e^{i\gamma_{l,\uparrow}}, e^{-i\gamma_{l,\uparrow}}]$ in the spin basis and we readily find the Wilson loop winding $W_{II} = W_{II}^{\mathcal{T}}$ with the winding number defined in Eq. (7).

When Rashba SOC is switched on adiabatically, the symmetry-protected windings of the spin-polarized Berry phase (7) are lifted into the spectral flow of the Wilson loop through an adiabatic mapping $\gamma_{l,\sigma} \mapsto \varphi_l$, leading again to $W_{II} = W_{II}^{\mathcal{T}}$ [67]. We verify this with several numerical examples in Fig. 6 with Wilson loop windings up to -5 (in Fig. 11 in Appendix B 3 we show one example of topological phase with a Wilson loop winding of $+7$). Starting from the spinless cases of Fig. 3, Fig. 6 shows the effect of first switching on s_z-preserving SOC (which opens a band gap over the whole BZ) and then switching on adiabatically Rashba SOC. The first row shows the band structures. The second row shows the flow of Wilsonian phases over the patch S_ρ as we smoothly sweep the base loop from $l_{\Gamma M}$ ($\theta = 0$) to $l_{\Gamma K}$ ($\theta = 1$) as illustrated in Fig. 5(b). The third row shows the flow of Wilsonian phases over the whole BZ as we sweep a base loop l_{g_2} parallel to the primitive reciprocal vector $\boldsymbol{b}_2$ over the whole BZ, i.e., we parametrize the BZ as $\mathrm{BZ} \cong \cup_{g_2\in[0,1]} l_{g_2}$ with $l_{g_2} \cong \{g_1\boldsymbol{b}_1 + g_2\boldsymbol{b}_2 | g_1 \in [0, 1]\}$. The flow then connects the Wilson loop over $l_{\Gamma M}$ ($g_2 = 0$), l_{MM} ($g_2 = 0.5$), and $l_{\Gamma M} + \boldsymbol{b}_1 \sim l_{\Gamma M}$ ($g_2 = 1$) (see Fig. 1). We have used the periodic gauge in the numerical computation of the Wilson loop which prevents large gauge transformations (see Appendix A 1). The only two allowed values $\overline{\varphi}(0) = 0$ and $\overline{\varphi}(0) = -\pi$ follow from the combined constraints of TRS and $C_{2z}\mathcal{T}$ symmetry that enforce the Wilson loop spectrum on $l_{\Gamma M}$ (and l_{MM}) to be $[+1, +1]$ or $[-1, -1]$. The other lattice symmetries enforce the reference Wilsonian phase on $l_{\Gamma K}$ to be $\overline{\varphi}(1) = \pm 2\pi/3$ (see derivation in the next section). In each case, we have written in the bottom of Fig. 6 the Wilson loop winding over the patch S_ρ ($W[S_\rho]$) for the choice $\overline{\varphi}(1) = -2\pi/3$ as the

[7]This arbitrariness is related to the fact that the real IRREP of a positive rotation within SO(2) is equivalent to the irreducible representation of a negative rotation. Similarly, $U_{\sigma_h}\mathcal{W}_l^* U_{\sigma_h}^\dagger = \mathcal{W}_l$ is a relation of equivalence between two Wilson loops with opposite phases.

[8]While the representative phase is smooth and takes value in a unbounded domain, i.e., $\varphi(\theta)/\pi \in \mathbb{R}$, the reference phases $\overline{\varphi}(0)$ and $\overline{\varphi}(1)$ are fixed constants within $[-\pi, \pi)$.

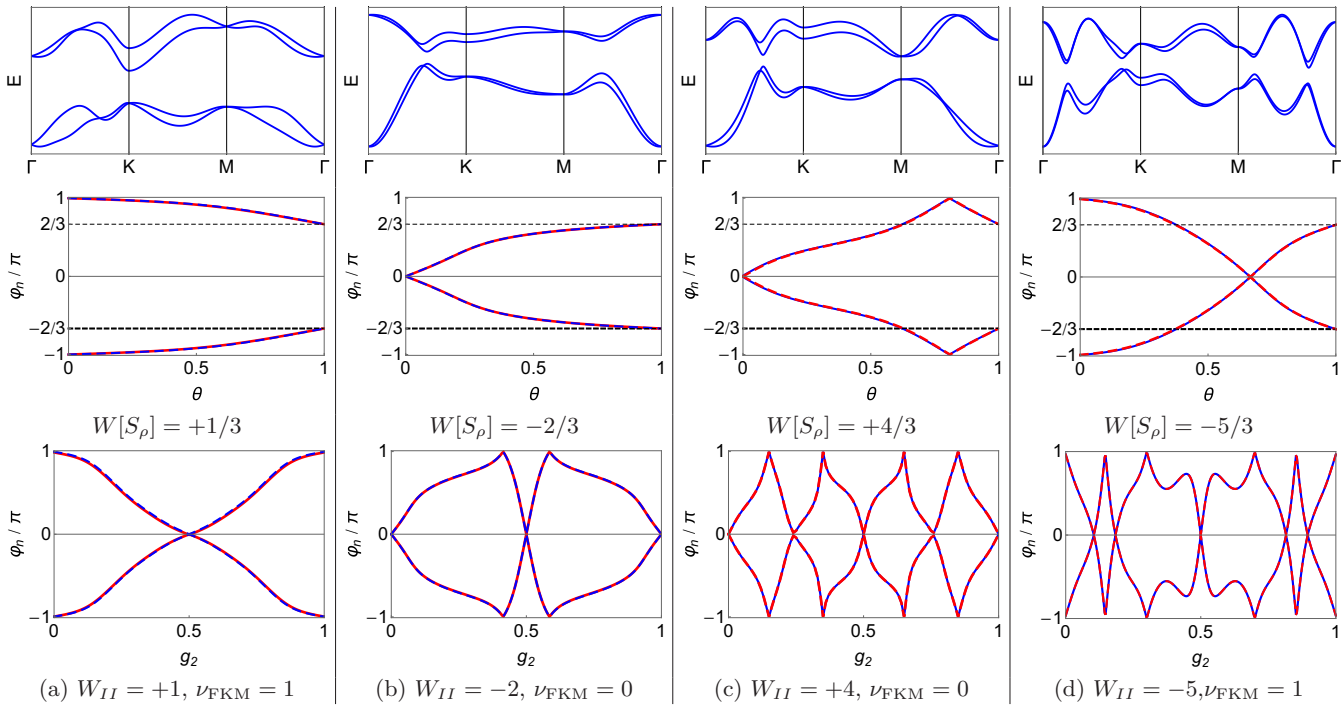

FIG. 6. Spinful topological phases obtained for SOC that break inversion symmetry only adiabatically. Columns (a)–(d) correspond to those of Fig. 3. First row: band structures along the high-symmetry lines of the BZ. Second row: spectral flow of the Wilson loop over one patch S_ρ parametrized by loop sections l_θ from $l_{\Gamma M}$ ($\theta = 0$) to $l_{\Gamma K}$ ($\theta = 1$). Third row: spectral flow of the Wilson loop over the whole BZ parametrized by loop sections $\{l_{g_2}\}_{g_2\in[0,1]}$ with $l_{g_2=0,1} = l_{\Gamma M}$ and $l_{g_2=0.5} = l_{MM}$. Blue (red) dashed lines give the Wilson loop of the two-band occupied (unoccupied) subspace. For each case, the Wilson loop winding over a sixth BZ patch $W[S_\rho]$ (computed with respect to reference Wilsonian phase marked by a thick black line), the Wilson loop winding W_{II}, and the Fu-Kane-Mele $\mathbb{Z}_2$ invariant are given. Importantly, the agreement between the second and the third rows confirms that the total winding of the Wilson loop over the BZ (protected by $C_2\mathcal{T}$ symmetry) does not depend on the parametrization of the flow.

reference Wilsonian phase, the winding of the Wilson loop over one HBZ (W_{II}), and the Fu-Kane-Mele $\mathbb{Z}_2$ invariant. We see a perfect confirmation of $W_{II} = 3W[S_\rho] = W_{II}^{\mathcal{I}} = W_I$ and $\nu_{FKM} = W[S_\alpha] \mod 2 = W_{II} \mod 2$. We note that the robustness of higher Wilson loop windings comes from the $C_{2z}\mathcal{T}$-symmetry protection of the crossings of Wilson loop branches (of Wilsonian phases) at 0 and $\pm\pi$. Furthermore, the agreement in Fig. 6 between the winding obtained from a symmetric flow over the patch S_ρ and from a nonsymmetric flow over the whole Brillouin zone confirms our claim that the Wilson loop winding protected by $C_2\mathcal{T}$ symmetry is independent of the parametrization of the flow.

Importantly, the spinful insulating phases always split an EBR [see the examples of Figs. 4(a) and 4(b) characterized by their IRREPs at the HSPs Γ, K, and M]. We give in Table II the relevant IRREPs for the generators of the little cogroups at the HSPs.[9] In the case with inversion symmetry we have the split EBR $B_1 + B_2$ where the allowed qBRs (quasiband representation [50]) $B_{1,2}$ can be formed from all the permutations among the IRREPs of Fig. 4(a). In the case without inversion symmetry (AII + L77), we have the split EBR $B_1 + B_2$ where now the qBRs are constrained by the compatibility relations among the IRREPs as $B_1 = (\overline{\Gamma}_{9(8)}, \overline{K}_6, \overline{M}_5)$ and $B_2 = (\overline{\Gamma}_{8(9)}, \overline{K}_4, \overline{K}_5, \overline{M}_5)$, i.e., only $\overline{\Gamma}_8$ and $\overline{\Gamma}_9$ can now be freely permuted. Furthermore, the Wilsonian phases can be interpreted as the expectation values of the position operator

TABLE II. Spinful IRREPs for the generators of the little cogroup [56] at the high-symmetry points Γ, K, and M, for L77 and L80 with TRS. Retrieved from the Bilbao Crystallographic Server [73]. We have marked as a superscript the parity eigenvalues ($\pm$) of the IRREPs of L80.

Γ	C_{6v}	D_{6h}	C_{6z}^+	m_x
	$\overline{\Gamma}_9$	$\overline{\Gamma}_9^{(+)}$	$\begin{pmatrix} e^{-i\pi/6} & 0 \\ 0 & e^{i\pi/6} \end{pmatrix}$	$\begin{pmatrix} i & 0 \\ 0 & -i \end{pmatrix}$
	$\overline{\Gamma}_8$	$\overline{\Gamma}_{11}^{(-)}$	$\begin{pmatrix} e^{i5\pi/6} & 0 \\ 0 & e^{-i5\pi/6} \end{pmatrix}$	$\begin{pmatrix} i & 0 \\ 0 & -i \end{pmatrix}$
K	C_{3v}	D_{3h}	C_{3z}^+	m_x
	$\overline{K}_4$	$\overline{K}_7$	-1	$-i$
	$\overline{K}_5$		-1	i
	$\overline{K}_6$	$\overline{K}_8$	$\begin{pmatrix} e^{i\pi/3} & 0 \\ 0 & e^{-i\pi/3} \end{pmatrix}$	$\begin{pmatrix} i & 0 \\ 0 & -i \end{pmatrix}$
M	C_{2v}	D_{2h}	C_{2z}^+	m_x
	$\overline{M}_5$	$\overline{M}_5^{(+)}$	$\begin{pmatrix} i & 0 \\ 0 & -i \end{pmatrix}$	$\begin{pmatrix} i & 0 \\ 0 & -i \end{pmatrix}$
	$\overline{M}_5$	$\overline{M}_6^{(-)}$	$\begin{pmatrix} i & 0 \\ 0 & -i \end{pmatrix}$	$\begin{pmatrix} i & 0 \\ 0 & -i \end{pmatrix}$

[9]In this work we have chosen the convention $C_n^+|\uparrow\rangle = e^{-i2\pi/n}|\uparrow\rangle$ and $C_n^+|\downarrow\rangle = e^{+i2\pi/n}|\downarrow\rangle$.

within the basis of Wannier functions generated only by the occupied Bloch eigenstates [24,25,39,41,68–72]. Therefore, whenever the Wilson loop has a symmetry-protected nontrivial winding there is an obstruction to the definition of a basis set of localized and *symmetric* Wannier functions since then the Wannier functions cannot have well-defined Wyckoff's positions. The symmetric condition means that the set of Wannier must be closed under all the symmetries of the system, otherwise some symmetry operations map some of these Wannier functions to the Wannier functions obtained from the Bloch functions of the unoccupied subspace. The offset of Eq. (7) marks that all the insulating phases of these symmetry classes must be topologically nontrivial. Hence, by considering a band structure that is composed only of the bands of a single EBR (here the four bands of the spinful honeycomb lattice), we quantitatively corroborate with a concrete example the claim of "topological quantum chemistry" [36,50] that whenever an EBR is split, the system must be topologically nontrivial. In Sec. VII we analyze the effect of adding (in the vector bundle sense) two EBRs and reveal the fragile topology of split EBRs.

VI. SPINFUL CASE WITH NONADIABATIC BREAKING OF INVERSION SYMMETRY

We now address the case beyond the adiabatic breaking of inversion symmetry. Phases with adiabatically broken inversion symmetry require Rashba SOC to be weak as compared to s_z-preserving SOC. When Rashba SOC is instead strong enough, additional topological phase transitions can occur. Putting aside the topological semimetallic phases at half-filling, the insulating phases of AII + L77(2*b*) always split the EBR into B_1 (with the IRREP $\overline{K}_6$ at K) and B_2 (with the IRREPs $\overline{K}_4$ and $\overline{K}_5$ at K). We thus continue the characterization of TQC [36,42,50] relating the split of an EBR and nontrivial topology.

Toward that aim, we use an alternative approach to the symmetry-protected quantization of Wilson loop spectra over $l_{\Gamma K}$ and $l_{\Gamma M}$ based on the (pseudo)spin locking at Γ, K, and M. This not only provides a more direct proof that $W_{II} = W_{II}^{\mathcal{I}}$ when inversion symmetry is broken adiabatically, but further nicely leads to the interpretation of the topological phases beyond the adiabatic breaking of inversion symmetry. The $\hat{z}$ axis of rotational symmetries at the HSPs Γ, K, and M naturally defines a quantization axis for the pseudospin degrees of freedom combining the orbital and the bare spin structures. Fewer band models have the additional feature that spin-flip terms vanish at some HSPs leading to a bare spin composition of the eigenstates that diagonalize the matrix representations of the rotation symmetries. For instance, all the spin-dependent terms vanish at Γ such that each Kramers doublet can be decomposed into pure spin components. By inspection of the Hamiltonian at Γ we find that the Bloch eigenstates form the doublets $(|\phi_{\Gamma_j}, \uparrow, \Gamma\rangle, |\phi_{\Gamma_j}, \downarrow, \Gamma\rangle)^T$, with $j = 1$ for the IRREP $\overline{\Gamma}_9$ ($\phi_{\Gamma_1} \propto \varphi_A + \varphi_B$) and $j = 4$ for the IRREP $\overline{\Gamma}_8$ ($\phi_{\Gamma_4} \propto \varphi_A - \varphi_B$), written in the basis that makes the matrix representation of the rotation symmetries at Γ diagonal (this is the symmetry Bloch basis defined in Appendix A 1). We find $\mathrm{diag}(e^{-i\pi/3}, e^{i\pi/3})$ as the representation of C_{3z}^+ symmetry for both doublets. By inspection of the Hamiltonian at K (say at K_1), we find that the doublet for the IRREP $\overline{K}_6$ can again be decomposed into pure spin components as $|\boldsymbol{\psi}_{\overline{K}_6}, K_1\rangle = (|\varphi_A, \uparrow, K_1\rangle, |\varphi_B, \downarrow, K_1\rangle)^T$ which gives $\mathrm{diag}(e^{i\pi/3}, e^{-i\pi/3})$ as the representation of C_{3z}^+ symmetry. The partner doublet at the inverted momentum $-K_1$ can be taken as $|\boldsymbol{\psi}_{\overline{K}_6}, -K_1\rangle = (|\varphi_B, \uparrow, -K_1\rangle, |\varphi_A, \downarrow, -K_1\rangle)^T$ such that it has the same matrix representation of rotations. We also verify that these two doublets are partners under TRS through

$$\langle \boldsymbol{\psi}_{\overline{K}_6}, -K_1|\mathcal{T}|\boldsymbol{\psi}_{\overline{K}_6}, K_1\rangle = \begin{pmatrix} 0 & -1 \\ 1 & 0 \end{pmatrix}\mathcal{K}. \tag{10}$$

The most general rotations of the doublets that preserve this form of the TRS correspond to a SU(2) transformation [74]. If we further want to preserve the diagonal form of the matrix representation of rotations, then only transformations of the form $\mathrm{diag}(e^{i\theta}, e^{-i\theta})$ are allowed. The Bloch eigenstates for the IRREPs $\overline{K}_4$ and $\overline{K}_5$ have a mixed spin structure due to the presence of spin-flip terms at K, i.e., we find

$$\begin{aligned} |\psi_{\overline{K}_4}, K_1\rangle &= (\omega|\varphi_A, \downarrow, K_1\rangle + |\varphi_B, \uparrow, K_1\rangle)/\sqrt{2}, \\ |\psi_{\overline{K}_5}, K_1\rangle &= (-\omega|\varphi_A, \downarrow, K_1\rangle + |\varphi_B, \uparrow, K_1\rangle)/\sqrt{2}, \end{aligned} \tag{11}$$

with $\omega = e^{i2\pi/3}$, and at the inverted momentum,

$$\begin{aligned} |\psi_{\overline{K}_4}, -K_1\rangle &= (-\omega^*|\varphi_A, \uparrow, -K_1\rangle + |\varphi_B, \downarrow, -K_1\rangle)/\sqrt{2}, \\ |\psi_{\overline{K}_5}, -K_1\rangle &= (\omega^*|\varphi_A, \uparrow, -K_1\rangle + |\varphi_B, \downarrow, -K_1\rangle)/\sqrt{2}. \end{aligned} \tag{12}$$

The C_{3z}^+-symmetry eigenvalue of the eigenstates $\overline{K}_4$ and $\overline{K}_5$ is -1. Allowing a rotation among the eigenstates, the basis $|\varphi_B, \uparrow, K_1\rangle \propto |\psi_{\overline{K}_4}, K_1\rangle + |\psi_{\overline{K}_5}, K_1\rangle$ and $|\varphi_A, \downarrow, K_1\rangle \propto |\psi_{\overline{K}_4}, K_1\rangle - |\psi_{\overline{K}_5}, K_1\rangle$ has a pure spin composition and conserves the C_{3z}^+-symmetry eigenvalue. Contrary to Γ and K, the eigenstates at M do not have a simple form and there is not a direct relation between the pseudospin basis that diagonalizes the representation of C_{2z} symmetry and the bare spin components.

In the spirit of Ref. [7], we characterize the topology of the two-band occupied subspace through the construction of a basis set of smooth (cell-periodic) Bloch functions $|\boldsymbol{v}, \boldsymbol{k}\rangle = (|v_1, \boldsymbol{k}\rangle, |v_2, \boldsymbol{k}\rangle)^T$ spanning the same Hilbert space. We call it a smooth frame for the occupied subspace. Such a frame always exists over one-dimensional loops in momentum space (actually, it always exists over the BZ by the vanishing of the first Chern class due to TRS) [75]. Furthermore, we can make it periodic over a loop that threads the BZ, i.e., where the final point of the loop is given by a shift of the base point by reciprocal lattice vector as for $l_{\Gamma K}$ and $l_{\Gamma M}$. Therefore, Wilson loops are diagonal and thus gauge invariant within this frame. More precisely, the Wilson loop operator takes the form $\widetilde{W}_l = \mathcal{P}_1 + \mathcal{P}_2$ with the product of projection operators written in the smooth and periodic frame $\mathcal{P}_i = \prod_{\boldsymbol{k}}^{l} |v_i, \boldsymbol{k}\rangle\langle v_i, \boldsymbol{k}|$ for $i = 1, 2$. The Wilson loop over $l_{\Gamma K}$, connecting Γ, K, and $\Gamma' = \Gamma + \boldsymbol{b}_1 + \boldsymbol{b}_2$, is then given by $\widetilde{\mathcal{W}}_{l_{\Gamma K}} = \langle \boldsymbol{v}, \Gamma'|\widetilde{W}_{l_{\Gamma K}}|\boldsymbol{v}, \Gamma\rangle = \mathrm{diag}(e^{i\varphi_1}, e^{i\varphi_2})$ where $\varphi_{1,2}$ are the Berry phases of each component of the frame. Similarly for $l_{\Gamma M}$ that connects Γ, M, and $\Gamma' = \Gamma + \boldsymbol{b}_1 + \boldsymbol{b}_2$.

In order to derive the symmetry-protected quantization of the Wilson loop spectrum over $l_{\Gamma K}$, we further require that the matrix representation of rotations at Γ, K, and Γ'

be diagonal within the smooth and periodic frame. We call this last condition the rotation-symmetric gauge. Following the parallel transport method of Soluyanov and Vanderbilt in Ref. [76], we have verified numerically that a smooth and periodic frame that also satisfies the rotation-symmetric gauge always exists in two-band subspaces.[10] While this points to a general proof of existence an analytical solution of the four-band Hamiltonian is missing and we leave it as future work. In the next section we argue that such a frame in general does not exist for a four-band subspace of a six-band Hamiltonian.

Within the smooth, periodic, and rotation-symmetric frame for the two-band occupied subspace, $\boldsymbol{v} = (v_1, v_2)$, the Wilson loop over $l_{\Gamma K} = l_b \circ l_a$, with the segments $l_a = l_{K_1 \leftarrow \Gamma}$ and $l_b = l_{\Gamma' \leftarrow K_1}$, is given by

$$\begin{aligned}\widetilde{\mathcal{W}}_{l_{\Gamma K}} &= \langle \boldsymbol{v}, \Gamma' | \widetilde{W}_b | \boldsymbol{v}, K_1 \rangle \langle \boldsymbol{v}, K_1 | \widetilde{W}_a | \boldsymbol{v}, \Gamma \rangle \\ &= \widetilde{\mathcal{W}}_b \widetilde{\mathcal{W}}_a = \tilde{R}_3^{\Gamma} \widetilde{\mathcal{W}}_a^{-1} \left(\tilde{R}_3^{K}\right)^{-1} \widetilde{\mathcal{W}}_a \\ &= \tilde{R}_3^{\Gamma} \begin{pmatrix} e^{-i\varphi_a} & 0 \\ 0 & e^{i\varphi_a} \end{pmatrix} \tilde{R}_3^{K} \begin{pmatrix} e^{i\varphi_a} & 0 \\ 0 & e^{-i\varphi_a} \end{pmatrix},\end{aligned}$$

where $\tilde{R}^{\bar{\boldsymbol{k}}}_{3(\bar{3})}$ is the diagonal matrix representation of the symmetry C_{3z}^{+} (C_{3z}^{-}) at the HSP $\bar{\boldsymbol{k}}$. Therefore,

$$\widetilde{\mathcal{W}}_{l_{\Gamma K}} = \begin{pmatrix} \xi_3^{\Gamma(1)} \xi_{\bar{3}}^{K(1)} & 0 \\ 0 & \xi_3^{\Gamma(2)} \xi_{\bar{3}}^{K(2)} \end{pmatrix}, \tag{13}$$

where $\xi^{\bar{\boldsymbol{k}}(n)}_{3(\bar{3})}$ are the C_{3z}^{+}- (C_{3z}^{-}-) symmetry eigenvalues of the nth component of the doublets at $\bar{\boldsymbol{k}} = \Gamma, K$, i.e., $\tilde{R}^{\bar{\boldsymbol{k}}}_{3(\bar{3})} = \mathrm{diag}(\xi^{\bar{\boldsymbol{k}}(1)}_{3(\bar{3})}, \xi^{\bar{\boldsymbol{k}}(2)}_{3(\bar{3})})$. Proceeding similarly for $l_{\Gamma M}$, we find

$$\widetilde{\mathcal{W}}_{l_{\Gamma M}} = \begin{pmatrix} \xi_2^{\Gamma(1)} \xi_{\bar{2}}^{M(1)} & 0 \\ 0 & \xi_2^{\Gamma(2)} \xi_{\bar{2}}^{M(2)} \end{pmatrix}, \tag{14}$$

where $\xi_{2(\bar{2})}$ are the C_{2z}^{+}- (C_{2z}^{-}-) symmetry eigenvalues.

It is now straightforward to obtain the symmetry-protected Wilson loop spectrum for all possible configurations of the two-band occupied subspace of the insulating phases of AII + L77(2b). For the qBR B_1, i.e., connecting $\overline{\Gamma}_9$ or $\overline{\Gamma}_8$ to $\overline{K}_6$, and assuming that within the smooth frame the spin components of the doublets are aligned at Γ and K (which we write $B_{1,\uparrow\uparrow}$), we find

$$\widetilde{\mathcal{W}}^{B_{1,\uparrow\uparrow}}_{l_{\Gamma K}} = \begin{pmatrix} e^{-i\frac{2\pi}{3}} & 0 \\ 0 & e^{i\frac{2\pi}{3}} \end{pmatrix}, \tag{15}$$

i.e., the smooth frame connects a doublet $(\uparrow, \downarrow)$ at Γ to a doublet $(\uparrow, \downarrow)$ at K. For the qBR B_2, i.e., connecting $\overline{\Gamma}_9$ or $\overline{\Gamma}_8$ to $(\overline{K}_4, \overline{K}_5)$, either spin alignments give

$$\widetilde{\mathcal{W}}^{B_2}_{l_{\Gamma K}} = \begin{pmatrix} -e^{-i\frac{\pi}{3}} & 0 \\ 0 & -e^{i\frac{\pi}{3}} \end{pmatrix} = \begin{pmatrix} e^{i\frac{2\pi}{3}} & 0 \\ 0 & e^{-i\frac{2\pi}{3}} \end{pmatrix}, \tag{16}$$

i.e., the smooth frame connects a doublet $(\uparrow, \downarrow)$ at Γ to a doublet $(\uparrow, \downarrow)$ or $(\downarrow, \uparrow)$ at K. When we compute the smooth and rotation-symmetric frame for B_2 we find that it is composed of pure spin components at K, i.e., $(v_1, v_2) \propto (\varphi_{B,\uparrow}(K_1), \varphi_{A,\downarrow}(K_1))$, which have the same rotation eigenvalue of -1 as the Bloch eigenstates under a C_{3z} rotation. We note, however, that the smooth frame is not really needed for B_2 since with $\tilde{R}_3^K = -\mathbb{I}$ we have [41] $\mathcal{W}_a^{-1} \tilde{R}_3^K \mathcal{W}_a = -\mathbb{I}$ which readily leads to the quantization of the Wilson loop $\mathcal{W}^{B_2}_{l_{\Gamma K}} = -\tilde{R}_3^{\Gamma}$ independently of the smoothness of the chosen Bloch frame (although it must satisfy the rotation-symmetric gauge in order for the rotation matrices to be diagonal). As for $l_{\Gamma M}$, since there is a single IRREP at M ($\overline{M}_5$) and the IRREPs at Γ ($\overline{\Gamma}_8, \overline{\Gamma}_9$) have identical C_{2z} eigenvalues, we find

$$\widetilde{\mathcal{W}}_{l_{\Gamma M}} = \begin{pmatrix} -i(\pm i) & 0 \\ 0 & i(\mp i) \end{pmatrix} = \begin{pmatrix} \pm 1 & 0 \\ 0 & \pm 1 \end{pmatrix}, \tag{17}$$

both allowed for B_1 and B_2. This result based on the construction of a smooth (periodic) and rotation-symmetric Bloch frame recovers the algebraic derivation of the quantization in Sec. IV based on the combined constraints of TRS and $C_{2z}T$ on the Wilson loop spectrum.

We conclude that $B_{1,\uparrow\uparrow}$ and B_2 give the same symmetry-protected reference Wilsonian phases $\overline{\varphi}(1) = \pm 2\pi/3$ [see definition in Eq. (8)]. Also, $\widetilde{\mathcal{W}}_{l_{\Gamma M}} = [\pm 1, \pm 1]$ leads to the symmetry-protected reference Wilsonian phases $\overline{\varphi}(0) = 0, \pm\pi$ in Eq. (8). We hence readily find a classification of the Wilson loop winding W_{II} [Eq. (9)] equivalent to Eq. (7) but here without assuming inversion symmetry. Having argued earlier that the classification of Eq. (7) must be conserved when inversion symmetry is broken only adiabatically (without closing the band gap), we then conclude that the condition of aligned spins at Γ and K (within the same smooth Bloch branch) in B_1 is equivalent to this adiabatic condition (i.e., adiabatic breaking of inversion symmetry) and $W_{II} = W_{II}^{\mathcal{I}}$.

Instead, taking the smooth frame and assuming that the spin components of the doublets of B_1 are flipped between Γ and K, which we write $B_{1,\uparrow\downarrow}$, we get

$$\widetilde{\mathcal{W}}^{B_{1,\uparrow\downarrow}}_{l_{\Gamma K}} = \begin{pmatrix} +1 & 0 \\ 0 & +1 \end{pmatrix}, \tag{18}$$

i.e., the symmetry-protected Wilsonian phase is now $\overline{\varphi}(1) = 0$. Therefore, taking this together with the unchanged $\overline{\varphi}(0) = 0, \pm\pi$ within Eq. (8) gives $W^{B_{1,\uparrow\downarrow}}[S_\rho] \in [\overline{\varphi}(1) - \overline{\varphi}(0)]/\pi \pmod 2 = \{0, \pm 1\} \pmod 2 = 0 \pmod 1 \cong \mathbb{Z}$. Hence, the set of symmetry-allowed Wilson loop windings (9) would now be $3\mathbb{Z} \ni W_{II}^{B_{1,\uparrow\downarrow}}$. While this could suggest that many more topological insulating sectors can be realized, we actually find only one additional topological insulating phase that is not contained in the classification of $B_{1,\uparrow\uparrow}$. Indeed, after exploring the phase diagram of the tight-binding model for the symmetry class AII + L77(2b) including up to the 10th layer of neighbors, we find that all the insulating phases beyond those classified by Eq. (7) have a zero winding of the Wilson loop for B_1, i.e., $W_{II}^{B_{1,\uparrow\downarrow}} = 0$. We show below that this phase exactly corresponds to the "fragile" topological phase that has been very recently reported in Ref. [51]. A formal proof that Γ-K spin-flip phases can only have a zero Wilson loop winding of B_1 is still missing and is kept for the future.

[10] Alternatively to Ref. [76] that uses a singular value decomposition, we mention the early construction of Ref. [91] based on a polar decomposition instead.

Let us analyze in more detail the two cases allowed by B_1. The pure spin structure of the doublets at Γ and K (for B_1) is a result of the vanishing of spin-flip terms of the four-band tight-binding Hamiltonian at Γ and K. On the one hand, the Γ-K spin-aligned configuration ($B_{1,\uparrow\uparrow}$) is naturally adiabatically connected to the inversion-symmetric case for which s_z is a good quantum number over the whole BZ. On the other hand, the Γ-K spin-flip configuration ($B_{1,\uparrow\downarrow}$) is allowed by Rashba spin-flip terms that unlock the quantization axis of the spins between Γ and K. We naturally expect that this is realized only when Rashba SOC is strong enough. Actually, since the rotation-symmetric gauge can always be satisfied by the smooth frame, any adiabatic transformation of the Hamiltonian cannot induce a transition between the spin-aligned and the spin-flipped configurations since it would require the continuous rotation of the spin-quantization axis for the doublet at K which is not supported by the four-band Hamiltonian of AII + L77($2b$). Therefore, we conclude that the phase with zero Wilson loop winding of B_1 can only be realized when Rashba SOC is strong enough to close and reopen the band gap. The classification of Wilson loop windings obtained from Eqs. (15) and (16) is in one-to-one correspondence with Eq. (7), which we have argued covers all the topological sectors that are adiabatically connected to the inversion-symmetric phases, i.e., with zero Rashba SOC. Then, since Eq. (18) implies a classification of the Wilson loop windings that is not contained in Eq. (7), it must relate to different topological sectors than Eq. (15). Therefore, the phase with a trivial B_1 subspace and captured by Eq. (18) cannot be adiabatically mapped to any of the inversion-symmetric phases.

Figure 7(a) shows one numerical example where the EBR is split into an occupied subspace with $B_1^a = (\overline{\Gamma}_9, \overline{K}_6, \overline{M}_5)$ and an unoccupied subspace with $B_2^a = (\overline{\Gamma}_8, \overline{K}_4, \overline{K}_5, \overline{M}_5)$. This example corresponds to the fragile topological phase of Ref. [51] (we have used the same parameters for comparison). Figure 7(b) shows one example where the EBR is split into $B_1^b = (\overline{\Gamma}_8, \overline{K}_6, \overline{M}_5)$ and $B_2^b = (\overline{\Gamma}_9, \overline{K}_4, \overline{K}_5, \overline{M}_5)$. In both cases, the Wilson loop spectrum of the B_1 occupied subspace has a zero winding (blue dashed lines), while the unoccupied subspace with B_2 conserves a nontrivial winding of $W_{II} = \pm 4$ (red lines). Reference [51] has shown the triviality of B_1^a in the example of Fig. 7(a) by computing, from the two occupied Bloch eigenstates, a set of two localized Wannier functions that are both centered at the lattice site C, and are mapped on each other under all the symmetries of the system (i.e., it is a closed basis set under symmetry). We arrive here at the same conclusion by straightforwardly computing the flow of Wilson loop revealing a zero Wilson loop winding for B_1. Furthermore, it is worth noting that these localized Wannier functions [51] exhibit a strong spin mixture. This nicely supports our spin-locking argument which predicts that the trivialized B_1 is characterized by a spin flip between Γ and K within the Bloch functions composing the smooth frame.

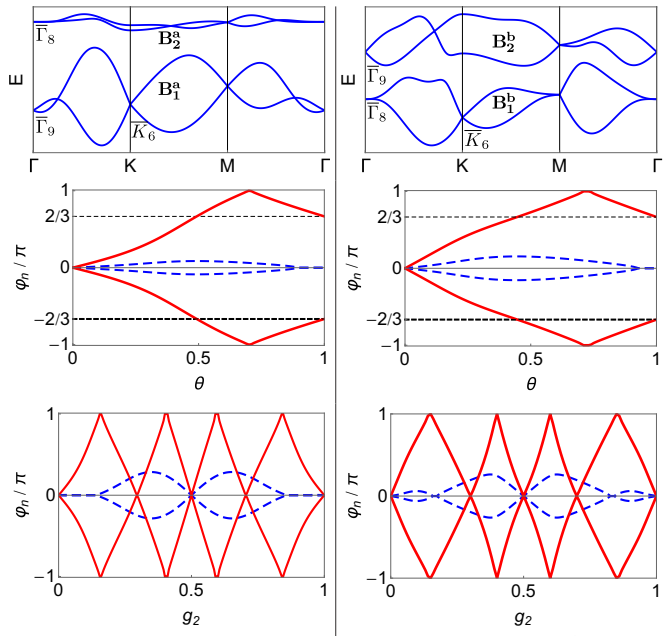

(a) $W^{B_1^a}[S_\rho] = W_{II}^{B_1^a} = 0$, $W_{II}^{B_2^a} = 4$, $\nu_{\mathrm{FKM}} = 0$ (b) $W^{B_1^b}[S_\rho] = W_{II}^{B_1^b} = 0$, $W_{II}^{B_2^b} = 4$, $\nu_{\mathrm{FKM}} = 0$

FIG. 7. Spinful topological phases with Rashba SOC breaking inversion symmetry nonadiabatically. First, second, and third rows are similar to Fig. 6. (a) EBR split as $B_1^a + B_2^a$ with $B_1^a = (\overline{\Gamma}_9, \overline{K}_6, \overline{M}_5)$ and $B_2^a = (\overline{\Gamma}_8, \overline{K}_4, \overline{K}_5, \overline{M}_5)$, with the parameters chosen as in Ref. [51] for comparison. (b) EBR split as $B_1^b + B_2^b$ with $B_i^b = B_i^a[\overline{\Gamma}_9 \leftrightarrow \overline{\Gamma}_8]$.

VII. SIX-BAND CASE

Having extensively treated the spinless two-band and spinful four-band cases, we now study the effect of including one extra sublattice site (C) located at the center of the unit cell, resulting in a total of six bands. The lattice sites C form a triangular lattice that corresponds to the Wyckoff's position $1a$ of L77.[11] Assuming a single orbital per site (e.g., an s orbital) the two spins on each site C give rise to the two-band EBR $B_1^a(1a) = (\overline{\Gamma}_9, \overline{K}_6, \overline{M}_5)$ [we could also form $B_1^b(1a) = (\overline{\Gamma}_8, \overline{K}_6, \overline{M}_5)$ for a different choice of orbital]. In this section we restrict ourselves to the coupling of the split EBR of the honeycomb lattice, i.e., $B_1 + B_2$ with $B_1 = B_1^{a/b}(2b)$ and $B_2 = B_2^{a/b}(2b)$ (see Fig. 7), with the EBR for the triangular lattice chosen as $B_1' = B_1^a(1a)$. Furthermore, we fix the occupied subspace as the two bands of B_1 and the unoccupied subspace as the four bands of $B_2 + B_1'$. Therefore, depending on the split of the EBR of the honeycomb lattice before the coupling, the qBR of the four-band unoccupied subspace is either compatible or incompatible with the set of IRREPs of a BR, that is an EBR or a sum of EBRs, of the symmetry class AII + L77. We write $B \sim \mathrm{BR}\,(\mathrm{EBR})$ when the quasiband representation B has a set of IRREPs that are compatible with

[11] We have derived our model using a generalization of Dresselhaus method for expanding global tight-binding models from the crystallographic space group [92]. Details of the method and the model will be given elsewhere. When restricted to the seventh layer of neighbors, our tight-binding model matches with the model given in Ref. [51].

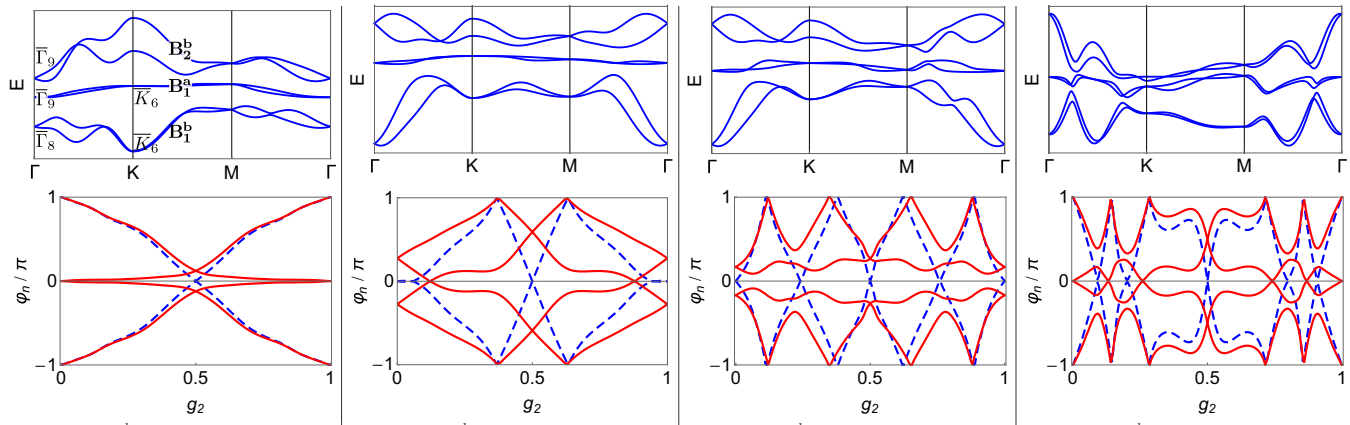

(a) $W_{II}^{B_1^b} = 1$, $\nu_{\mathrm{FKM}} = 1$, $\nu_{21'} = 1$ (b) $W_{II}^{B_1^b} = 2$, $\nu_{\mathrm{FKM}} = 0$, $\nu_{21'} = 2$ (c) $W_{II}^{B_1^b} = 4$, $\nu_{\mathrm{FKM}} = 0$, $\nu_{21'} = 0$ (d) $W_{II}^{B_1^b} = 5$, $\nu_{\mathrm{FKM}} = 1$, $\nu_{21'} = 1$

FIG. 8. Six-band topological phases from the coupling of the split EBR $B_1 + B_2 = B_1^b(2b) + B_2^b(2b)$ (Fig. 6) with $B_1' = B_1^a(1a)$. Each six-band phase is generated from the corresponding four-band phase of Fig. 6. First row: band structures where all columns have the same energy ordering of IRREPs as in column (a). Second row: Wilson loop flows over the BZ for the occupied subspace B_1^b (blue dashed line) and for the unoccupied subspace $B_1^a + B_2^b$ (red line). For each case we give the Wilson loop winding (W_{II}) and the Fu-Kane-Mele invariant (ν_{FKM}) of the two-band occupied subspace, as well as the four-band index $\nu_{21'} \in \mathbb{Z}_3$ protected by TRS and $C_{2z}\mathcal{T}$.

a BR (EBR), and $B \not\sim$ BR when it is not. In the following examples, we have $B_2 + B_1' = B_2^a(2b) + B_1^a(1a) \sim$ EBR and $B_2 + B_1' = B_2^b(2b) + B_1^a(1a) \not\sim$ BR.

A. Numerical results

Figures 8 and 9 show six-band topological insulating phases generated through the coupling of the honeycomb lattice sites (Wyckoff's position $2b$ of L77) with the triangular lattice sites (Wyckoff's position $1a$ of L77). In Figs. 8 and 9(b) the split EBRs of the honeycomb lattice before coupling were all chosen as $B_1^b + B_2^b$. Since the results generated from the other choice of split EBRs, i.e., $B_1^a + B_2^a$, lead to qualitatively

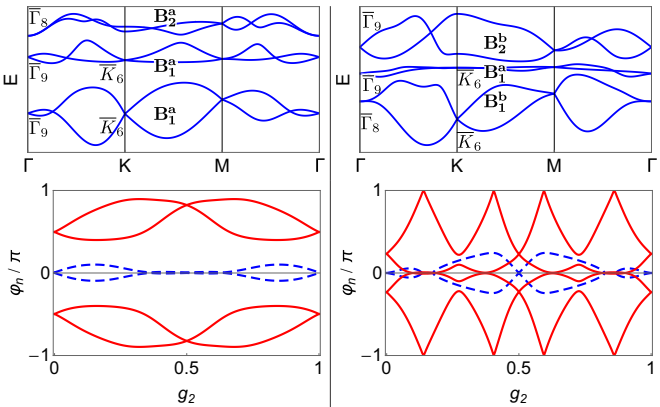

(a) $W_{II}^{B_1^a} = 0$, $\nu_{\mathrm{FKM}} = 0$, $\nu_{21'} = 0$ (b) $W_{II}^{B_1^b} = 0$, $\nu_{\mathrm{FKM}} = 0$, $\nu_{21'} = 0$

FIG. 9. Similar to Fig. 8, but here the six-band topological phases are obtained from the four-band phases of Fig. 7 where inversion symmetry is broken nonadiabatically through Rashba SOC. (a) Split EBR $B_1^a + B_2^a$, corresponding to the case discussed in Ref. [51]. (b) Split EBR $B_1^b + B_2^b$.

identical conclusions, we give them in Appendix D (Fig. 12). Figure 9(a) is the analog to Fig. 9(b) for the split EBR $B_1^a + B_2^a$.

The six-band phases of Fig. 8 are obtained column by column [Figs. 8(a)–8(d)] from the respective four-band topological phases of Fig. 6 where inversion symmetry was broken adiabatically. In Fig. 9 six-band phases are obtained from the four-band topological phases of Fig. 7 where Rashba SOC had broken inversion symmetry nonadiabatically. The first row in Figs. 8 and 9 has band structures with the same energy ordering of the IRREPs as shown in the first column. The second row in Figs. 8 and 9 gives the flow of Wilsonian phases over the whole BZ for the two-band occupied subspace (blue dashed line) and the four-band unoccupied subspace (red full line). In each case, we give the Wilson loop winding W_{II} [Eq. (9)] and the Fu-Kane-Mele invariant ν_{FKM} of the occupied subspace.

Analyzing the results we find, on the one hand, when comparing Fig. 8 with Fig. 6, and Fig. 9 with Fig. 7, that the topology of the two-band occupied subspace is preserved when two extra bands are included in the unoccupied subspace. On the other hand, the nontrivial Wilson loop winding of the two-band unoccupied subspace is sometimes lost when it is imbedded into the four-band Wilson loop of the six-band system. In particular, we observe that every crossing between Wilsonian branches is avoided away from the phases 0 and $\pm\pi$ where the degeneracies are protected by $C_{2z}\mathcal{T}$ symmetry, and away from the loops $l_{\Gamma M}$ ($g_2 = 0, 1$) and l_{MM} ($g_2 = 0.5$) where the degeneracies are protected by TRS. In total, we count three distinct Wilson loop patterns of the four-band subspace: (i) each Wilsonian phase winds by $\pm\pi$ over the whole BZ [Figs. 8(a) and 8(d)], (ii) each Wilsonian phase winds by $\pm 2\pi$ over the whole BZ [Fig. 8(b)], (iii) zero winding of each Wilsonian phase [Figs. 8(c), 9(a), and 9(b)]. This suggests a $\nu_{21'} \in \mathbb{Z}_3$ classification of the four-band subspaces protected by TRS and $C_{2z}\mathcal{T}$ symmetry, where the new index $\nu_{21'}$ refers

to the magnetic point group $21' = C_2 \times \{E, \mathcal{T}\}$ that contains TRS and $C_{2z}\mathcal{T}$ symmetry.

For completeness, we show in Fig. 13(a) of Appendix D one example with B_2^a as the two-band occupied subspace with $W_{II}^{B_2^a} = 4$. The result in this case is analog to Fig. 8(c) with a nonzero Wilson loop winding of the occupied subspace and a vanishing Wilson loop winding of the four-band unoccupied subspace. We also show as a reference in Fig. 13(b) an example with $B_1' = B_1^a(1a)$ ($W_{II}^{B_1'} = 0$) chosen as the occupied subspace. This case has no winding of the Wilson loops.

Importantly, in all the six-band results of Figs. 8, 9, and 13, we have included the two extra trivial bands B_1' from above in energy such that they had to cross the two bands B_2 nonadiabatically, i.e., closing the band gap. However, we have checked that in all the cases the two-band Wilson loop winding of B_2 and the zero winding of B_1' are conserved separately whenever there is an energy gap between them. Therefore, while there is no $\mathbb{Z}$-type Wilson loop winding of the four-band subspaces, the Wilson loop winding of two-band subspaces is robust as long as the two bands are separated from the other bands by an energy gap above and below.

VIII. DISCUSSION

Based on the six-band numerical results of the previous section, we discuss here in detail the topology of two- and four-band subspaces for the symmetry class AII + L77. We introduce the distinction between stable, unstable, and fragile topologies within vector bundle theory, and relate these to the topology of split EBRs. We then conclude that in the many-band limit the stable Wilson loop winding is determined only by the Fu-Kane-Mele $\mathbb{Z}_2$ invariant implying that further stable topological phases must belong to the class of higher-order topological insulators [52,53]. For completeness, we also briefly discuss the effect of breaking $C_{2z}\mathcal{T}$ symmetry, and TRS, from which Chern insulators with high Chern numbers can be formed.

A. Stable, unstable, and stably trivial or "fragile" topology

The topological classification of band structures, i.e., of vector bundles, can be recast in terms of homotopy groups of the classifying spaces of the Hamiltonian, i.e., the complex Grassmannian $\mathrm{Gr}_m(\mathbb{C}^n)$ where m is the number of occupied bands and n is the total number of bands [23,77–79] The homotopy groups of a space X generally depend on the dimension of X. The classical example is given by the homotopy groups of the d-dimensional spheres, i.e., $\pi_{k+d}(\mathbb{S}^d)$. When the dimension d is large enough ($d \geqslant k+2$), the homotopy groups are independent of d, i.e., one says that the homotopy groups are *stable* [80]. On the contrary for small d, the homotopy groups strongly depend on d and are called *unstable*. For instance, $\pi_3(\mathbb{S}^2) = \mathbb{Z}$ (unstable), while $\mathbb{Z}_2 = \pi_4(\mathbb{S}^3) = \pi_5(\mathbb{S}^4)\ldots$ (stable) [80].

The prototypical example of stable topology in the physics literature are the Chern insulators, i.e., their topology is unaffected by adding a trivial band to the occupied or the unoccupied subspaces, indeed we have $\pi_2(\mathrm{Gr}_1(\mathbb{C}^2)) = \pi_2(\mathrm{Gr}_m(\mathbb{C}^n)) = \mathbb{Z}$. Examples of unstable topology are three-dimensional two-band systems, called Hopf insulators, i.e., the classifying space is $\mathrm{Gr}_1(\mathbb{C}^2) \cong \mathbb{S}^2$ and $\pi_3(\mathbb{S}^2) = \mathbb{Z}$ [81,82]. By adding one band to a Hopf insulator, the dimension of the classifying space is increased and the Hopf topology is lost, as $\pi_3(\mathrm{Gr}_{1,2}(\mathbb{C}^3)) = 0$. Further physical example of unstable topologies is discussed in Ref. [61].

The example of the tangent bundle ($T\mathbb{S}^d$) and the normal bundle ($N\mathbb{S}^d$) of a d sphere give yet another possibility. Whenever $d \neq 1, 3, 7$, the tangent bundle is nontrivial, while the normal bundle is always trivial [83]. It turns out that the "addition" (the direct sum) of the tangent and the normal bundles gives a trivial bundle, i.e., $T\mathbb{S}^d \oplus N\mathbb{S}^d \cong \mathbb{S}^d \times \mathbb{R}^{d+1}$. Therefore, a nontrivial bundle ($T\mathbb{S}^d$, $d \neq 1, 3, 7$) can be combined with a trivial one ($N\mathbb{S}^d$) through a direct sum, resulting in a trivial bundle. In this case, one says that the tangent bundle is *stably trivial*, i.e., the (vector) bundle is trivialized by adding one trivial bundle [83]. The above terminology can be directly transferred to the characterization of the topology of band structures, where the direct sum of two vector bundles is interpreted as the grouping of two band subspaces, i.e., by discarding the energy gap between the two sets of bands and treating them as a single higher-dimensional subspace. Importantly, we call the topology of a band subspace "fragile" when it is stably trivial in the sense of the above example from vector bundle theory.

In the following, we distinguish between three kinds of stability. We call it stable topology of an N-band occupied subspace when it is robust under the addition of extra trivial bands in the occupied or unoccupied subspace (e.g., Chern insulators). We call it unstable topology of a system when it is lost under the addition of extra trivial bands either in the occupied or in the unoccupied subspace (e.g., Hopf insulators). We call it fragile topology of an N-band subspace when it is conserved under the inclusion of extra trivial bands separated from the N-band subspace by a band gap but lost if the extra bands are added nonadiabatically (i.e., closing the band gap) with respect to the N-band subspace. We argue in this section that, based on the numerical results of Sec. VII A, the two-band topology of split EBRs of the honeycomb lattice is fragile for most of the topological sectors identified in the single EBR. In particular, we show that the topology of four-band subspaces of the symmetry class AII + L77($2b + 1a$) is independent of whether or not their set of IRREPs is compatible with the set of IRREPs of an EBR or a sum of EBRs of AII + L77($2b + 1a$), while two-band subspaces originating from a split EBR conserve their nonzero Wilson winding.

B. Two-band subspace

We start with a discussion of two-band subspaces, i.e., two bands separated from all the other bands by an energy gap above and below. Let us first characterize the bands of the triangular lattice alone. Its band structure is made of the single EBR $B_1^a(1a) = (\overline{\Gamma}_9, \overline{K}_6, \overline{M}_5)$ that cannot be split because of the Kramers degeneracies at the TRIMPs due to TRS. A basis of smooth Bloch functions that spans the two-band Hilbert space is readily given by $\{|\varphi_C, \uparrow, \boldsymbol{k}\rangle, |\varphi_C, \downarrow, \boldsymbol{k}\rangle\}$ which is the Fourier trivialization of the total Bloch bundle [59]. Hence, the Berry phase of each component is vanishing over any chosen loop and the two-band Wilson loop has zero

winding.[12] Similarly, the triviality of any unsplit EBR is obvious as it is for any band structure where the number of occupied bands equals the total number of bands.

Let us now characterize the two-band occupied subspace of the six-band case introduced in Sec. VII. First of all, in the case when the occupied subspace is spanned by B_2, we readily find a classification of the Wilson loop windings that matches with Eq. (7) as is the case from Eq. (16). Indeed, as explained below Eq. (16), B_2 has $\tilde{R}_3^K = -\mathbb{I}$ which readily leads to a symmetry-protected quantization of the Wilson loop spectrum [41] over $l_{\Gamma K}$ given by Eq. (16) and leading to the classification of Wilson loop windings of Sec. VI, i.e., $W_{II}^{B_2} \in \pm\mathbf{1} + 3\mathbb{Z}$.

When the occupied subspace is spanned by B_1, as chosen in Sec. VII A in Figs. 8 and 9, we have to generalize the discussion of Sec. VI that was based on the spin locking of the doublets at Γ and K of a smooth, periodic, and rotation-symmetric frame spanning the two-band occupied subspace of the four-band system and over base loops of the BZ. In the six-band case, this approach is straightforwardly generalized by considering the pseudospin locking of the doublets at Γ and K. Indeed, the axis of rotation symmetries at these HSPs gives a favored quantization axis of the pseudospin degrees of freedom, i.e., only in that spin basis is the matrix representation of rotations' diagonal. Actually at Γ, as a result of the fact that we only consider a single orbital per site, all spin-flip terms still vanish, leading to a pure spin decomposition of the doublets $\overline{\Gamma}_{8(9)}$. At K, however, the six-band tight-binding model has open spin-flip channels leading to a pseudospin structure of the doublets $\overline{K}_6$. For completeness, we give in Appendix C the exact expression of the Bloch eigenstates of the six-band model at Γ and K.

Assuming the existence of a smooth, periodic, and rotation-symmetric frame of (cell-periodic) Bloch functions that span the two-band occupied subspace B_1 over base loops (see Sec. VI), we obtain the same classification as in the four-band model derived in Sec. VI. The difference now is that the smooth frame connects the spin components of the doublet $\overline{\Gamma}_{8(9)}$ at Γ to the pseudospin components of the doublets $\overline{K}_6$ at K, while the dichotomy of Γ-K spin to pseudospin aligned or Γ-K spin to pseudospin flipped still holds. Again using the parallel transport method of Ref. [76], we have verified that such a smooth and rotation-symmetric frame always exists for any two-band subspace of the six-band model. We then conclude that the symmetry-protected quantization of two-band Wilson loop spectrum over $l_{\Gamma K}$ derived in Sec. VI is preserved in the six-band case and thus leads to the same classification of the occupied subspace B_1, i.e., $W_{II}^{B_1} \in \{\pm\mathbf{1} + 3\mathbb{Z}, \mathbf{0}\}$.

[12]It is important to note that $B_1^a(1a)$ contains simple point nodes at the TRIMPs that are characterized by nontrivial Berry phases. Considering a two-band model for $B_1^a(1a)$ (i.e., the triangular lattice sites C with spins) at half-filling, the single occupied band has the Bloch eigenstate $|\psi_{occ}, \boldsymbol{k}\rangle \propto -e^{i\theta(\boldsymbol{k})}|\varphi_C, \uparrow, \boldsymbol{k}\rangle + |\varphi_C, \downarrow, \boldsymbol{k}\rangle$, where $\theta(\boldsymbol{k}) = \sqrt{h_{C\uparrow,C\downarrow}(\boldsymbol{k})/h_{C\uparrow,C\downarrow}(\boldsymbol{k})^*}$ with $h_{C\uparrow,C\downarrow}$ the off-diagonal matrix element of the 2×2 tight-binding Hamiltonian. We readily find that the phase $\theta(\boldsymbol{k})$ imposes a nontrivial Berry phase over any loop that encircles the simple point nodes at the TRIMPs.

At this point, it is reasonable to postulate the existence of a smooth, periodic, and rotation-symmetric frame for every two-band occupied subspace of the symmetry class AII + L77 and over base loops of the BZ, thus leading to the same and unique classification independently of the number of unoccupied bands. The only difference in the most general case is that spin-flip terms can also be nonzero at Γ (i.e., if each lattice site is the host of multiple electronic orbitals with opposite parities), thus leading to a pseudospin structure of the Bloch eigenstates at Γ as well. This, however, does not change the dichotomy between the phases with a pseudospin aligned between Γ and K and the phases where the pseudospin is flipped between Γ and K. The same result applies for any two-band subspace that originates from a split EBR as long as it remains separated from the other bands by an energy gap above and below. We leave the formal proof of the existence of a smooth, periodic, and rotation-symmetric frame of any two-band subspace over a base loop for the future.

We conclude that the obstructed $\mathbb{Z}$-type topological classification, i.e., $W_{II} \in \{\pm\mathbf{1} + 3\mathbb{Z}, \mathbf{0}\}$, of any two-band subspace of the symmetry class AII + L77 is stable under the addition of arbitrary many bands in the complement band subspace and as long as a band gap around the two-band subspace is preserved. This is schematically represented in Fig. 10 showing that two-band occupied subspaces, with zero Wilson loop winding marked in white and nonzero Wilson loop windings marked in green, have their topology unchanged after the coupling with extra bands separated by a band gap. This is true for all six-band models computed in this work and shown in Figs. 8 and 9 in Sec. VII A and Fig. 12 in Appendix D.

C. Four-band subspace

We now turn to the topology of the four-band subspaces in the six-band case. Starting from a split EBR of the honeycomb lattice $B_1 + B_2$ with a known topology, we couple it with the trivial EBR of a triangular lattice B_1' and characterize the topology of the four-band unoccupied subspace $B_{2/1} + B_1'$ where we either choose B_1 or B_2 as the occupied subspace. Depending on the way the EBR of the honeycomb lattice splits, the four-band unoccupied subspace has a set of IRREPs that either are compatible with an BR (i.e., an EBR or a sum of EBRs) of AII + L77, or it is not. The combinatorial possibilities for the four-band subspaces of the six-band case are

$$\begin{aligned}
B_2^a(2b) + B_1^a(1a) &= (\overline{\Gamma}_9 + \overline{\Gamma}_8, \overline{K}_4 + \overline{K}_5 + \overline{K}_6, 2\overline{M}_5) \\
&\sim \text{EBR} = B_1^{a(b)}(2b) + B_2^{a(b)}(2b), \\
B_2^b(2b) + B_1^a(1a) &= (2\overline{\Gamma}_9, \overline{K}_4 + \overline{K}_5 + \overline{K}_6, 2\overline{M}_5) \\
&\not\sim \text{BR}, \\
B_1^a(2b) + B_1^a(1a) &= (2\overline{\Gamma}_9, 2\overline{K}_6, 2\overline{M}_5) \\
&\sim \text{BR} = B_1^a(1a) + B_1^a(1a), \\
B_1^b(2b) + B_1^a(1a) &= (\overline{\Gamma}_9 + \overline{\Gamma}_8, 2\overline{K}_6, 2\overline{M}_5) \\
&\sim \text{BR} = B_1^a(1a) + B_1^b(1a).
\end{aligned} \tag{19}$$

The conclusions of this section are the same if we choose the extra bands B_1' as $B_1^b(1a) = (\overline{\Gamma}_8, \overline{K}_6, \overline{M}_5)$ instead of $B_1^a(1a) = (\overline{\Gamma}_9, \overline{K}_6, \overline{M}_5)$.

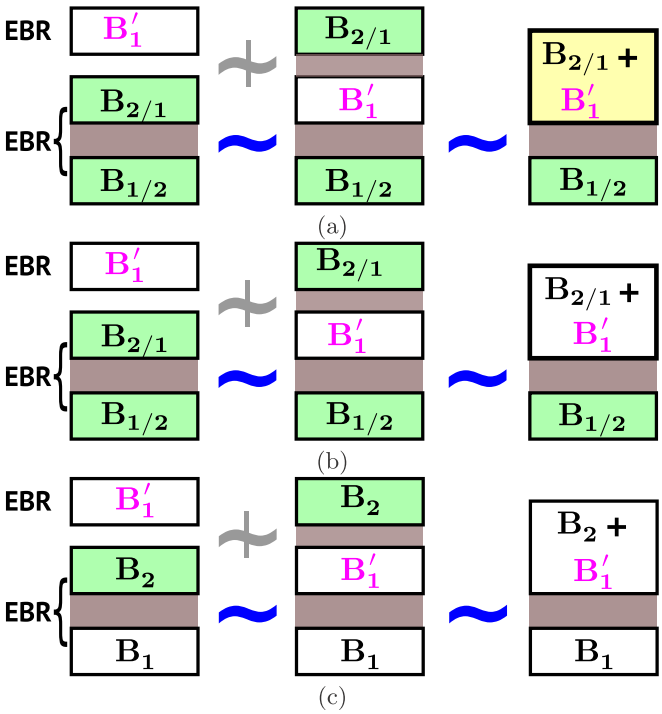

FIG. 10. Fragile topology of the split EBR of the honeycomb lattice $B_1 + B_2$, with $B_1 = B_1^{a/b}(2b)$ and $B_2 = B_2^{a/b}(2b)$, under the coupling with the trivial EBR of the triangular lattice $B_1' = B_1^{a/b}(1a)$. Two-band (four-band) subspaces with nonzero Wilson loop winding are colored in green (yellow), otherwise in white. In (a) and (b) we choose either B_1 or B_2 as the two-band occupied subspace of the six-band insulating phases, in (c) it can only be B_1. The band gaps are drawn in brown. The blue ∼ marks that the coupling is adiabatic, i.e., without closing the band gap, while the barred gray marks a nonadiabatic coupling (i.e., closing the band gap). (a) Reveals a stable topology of the split EBR (i.e., here for a nonzero Fu-Kane-Mele invariant). (b), (c) Reveal a fragile topology of the split EBR (i.e., nonzero two-band Wilson loop winding but with a zero Fu-Kane-Mele invariant). (c) Corresponds to the example given in Ref. [51], and here in Fig. 9.

We then ask how the topology of the four-band subspace, given in terms of the winding of the four-band Wilson loop over the BZ, is related to the known topology of split EBRs (Sec. VI). From the numerical results of Sec. VII A in Figs. 8 and 9, and in Fig. 12 of Appendix D) we conclude that the two-band topology is in general fragile when imbedded into a four-band subspace irrespectively of whether or not the set of IRREPs (of the four-band subspace) is compatible with a BR.

For clarity, let us summarize our findings in Fig. 10, where nontrivial two-band (four-band) Wilson loop windings are colored in green (yellow). In the left column, we show the schematic EBRs and their topologies before the coupling. In the middle column, we show the topology of the coupled EBRs, after that the EBR B_1' has crossed from above and nonadiabatically[13] the upper half of the split EBR $B_1 + B_2$. In the right column we show the topology when there is no gap between B_1' and the upper half of $B_1 + B_2$, hence characterizing the intrinsic four-band topology of the unoccupied subspace.

Two possibilities are encountered after coupling a split EBR with an extra EBR, as shown in Fig. 10: (a) both occupied and unoccupied subspaces have stable topology, (b) and (c) both occupied and unoccupied subspaces have fragile topology [where (c) corresponds to the special case found by Ref. [51]]. Only for special values of the two-band Wilson loop winding before the coupling do we find a topological four-band unoccupied subspace, e.g., Figs. 8(a), 8(b), and 8(d) and Figs. 12(a), 12(b), and 12(d). Therefore, the obstructed $\mathbb{Z}$-type classification of two-band Wilson loop winding is lost in general in four-band Wilson loops. We hence conclude that the topology of split EBRs is generically fragile when imbedded in many-band structures.

We further show that even when the unoccupied subspace has a set of IRREPs incompatible with EBRs its topology can be fragile with a vanishing four-band Wilson loop winding. Let us first consider for instance the four-band unoccupied subspace of Fig. 8(c) that has a zero Wilson loop winding. Indeed, the crossings at 0 have been lifted and the crossings at $\pm\pi$ can be removed two by two through an adiabatic deformation of the Wilson loop branches. This case corresponds to Fig. 10(b) for the initial split EBR $B_1^b + B_2^b$. Similarly, the four-band unoccupied subspace of Fig. 9(b) has a zero Wilson loop winding (here the crossings at 0 and at $\pm\pi$ can both be removed two by two through an adiabatic deformation of the Wilson loop branches). This case corresponds to Fig. 10(c) for the same initial split EBR. Reversely, we also show that when the unoccupied subspace has a set of IRREPs that is compatible with EBRs its topology can be nontrivial, e.g., Figs. 12(a), 12(d), and 12(b) which have a nonzero Wilson loop winding. These cases correspond to Fig. 10(a) for the initial split EBR $B_1^a + B_2^a$. These results greatly generalize the recent observation of a "fragile topology" in Ref. [51].

We have checked numerically that the four-band Wilson loop spectra in the six-band case are not quantized over $l_{\Gamma K}$ contrary to the two-band Wilson loop spectra. Furthermore, we have also checked numerically using the Soluyanov-Vanderbilt's smooth gauge construction [76] that the four-band subspaces do not support a smooth and periodic frame that, at the same time, also satisfies the rotation-symmetric gauge (making rotation matrix representations diagonal). Therefore, the Wilson loop spectrum of four-band subspaces is generically not quantized by symmetry and we do not expect the $\mathbb{Z}$-type Wilson loop winding of the two-band subspaces to be stable. This confirms the homotopy classification of Wilson loop flows of Sec. IV. We give a more detailed discussion in Appendix E.

We conclude with the characterization of the preserved four-band topologies. We observed in Sec. VII A that the crossings of Wilsonian branches that remain are those at 0 and $\pm\pi$, as they are protected by $C_{2z}\mathcal{T}$ symmetry, and the Kramers degeneracies over $l_{\Gamma M}$ ($g_2 = 0, 1$) and l_{MM} ($g_2 = 0.5$), as they are protected by TRS. This readily leads to a $\nu_{21'} \in \{0, 1, 2\} \cong \mathbb{Z}_3$ classification of the four-band subspaces with the index $\nu_{21'}$ being protected by the magnetic point group $21' = C_2 \times \{E, \mathcal{T}\}$ that contains TRS and $C_{2z}\mathcal{T}$ symmetry. In particular, we find that the two-band Wilson loop winding

[13] Any inversion in energy of two qBRs with distinct IRREPs must close the energy gap between them.

before the coupling directly determines the four-band index $\nu_{21'}$ according to

$$\begin{aligned} W_{II}^{B_{2/1}} \bmod 2 = 1 &\Rightarrow \nu_{21'} = 1, \\ W_{II}^{B_{2/1}} \bmod 2 = 0 \text{ and } W_{II}^{B_{2/1}} \bmod 4 = 0 &\Rightarrow \nu_{21'} = 0, \\ W_{II}^{B_{2/1}} \bmod 2 = 0 \text{ and } W_{II}^{B_{2/1}} \bmod 4 = 2 &\Rightarrow \nu_{21'} = 2. \end{aligned} \tag{20}$$

The Fu-Kane-Mele $\mathbb{Z}_2$ invariant is then readily given through $\nu_{\mathrm{FKM}} = \nu_{21'} \mod 2$.

D. Toward the many-band limit

If an extra trivial two-band subspace $B_1^{a/b}$ is added to the occupied subspace, the topological features of the four-band occupied subspace are similar to the four-band unoccupied subspace described above. If instead the extra trivial two-band subspace is added to the four-band unoccupied subspace, only two types of Wilson loop flow are allowed for the six-band subspace, namely, either a Wilson loop flow with zero winding (gapped Wilson bands) or with a complete winding (no gap in the Wilson bands). Hence, $\nu_{21'} \in \mathbb{Z}_3$ should be understood again as a fragile topology. We also conclude that only a nontrivial Fu-Kane-Mele $\mathbb{Z}_2$ invariant guarantees a complete winding of the Wilson loop in the many-band limit. As a consequence, the further stable topological phases that have been predicted heuristically in Ref. [43] must be characterized by topological invariants that are not directly related to the Wilson loop winding and fall in the class of the higher-order topological insulators [52,53]. This falls beyond the scope of this work and it will be explored in detail elsewhere.

E. Breaking $C_{2z}\mathcal{T}$ symmetry, and TRS

It is now straightforward to address the breaking of the antiunitary symmetries. When $C_{2z}\mathcal{T}$ symmetry is broken while conserving TRS the degeneracies of the Wilson loop at 0 and $\pm\pi$ are lifted and only two types of Wilson loop patterns survive which correspond to the two values of the Fu-Kane-Mele $\mathbb{Z}_2$ invariant. When TRS is broken adiabatically, the Kramers degeneracies of the Wilson loop over $l_{\Gamma M}$ and l_{MM} are also lifted and there is no winding of the Wilson loop left. This can be easily understood from the fact that any two- or four-band subspaces can be decomposed into pair(s) of Chern bands with opposite Chern numbers [7], which cancel each other if the number of occupied bands is unchanged when breaking TRS. If TRS symmetry is broken nonadiabatically, nonzero Chern numbers can be generated. In particular, let us start with a two-band occupied subspace with a high winding of its Wilson loop. Then, by breaking TRS and keeping a single occupied band, we are guaranteed to generate a Chern insulator with a correspondingly high Chern number. Therefore, the two-band Wilson loop winding directly determines the one-band Chern number under the breaking of TRS.

IX. CONCLUDING REMARKS

In this work we have studied the relation between Wilson loop flows and symmetry-protected topology of band structures. Apart from elucidating nodal points by generalizing Berry curvature arguments to include space-group symmetries, thereby outlining a unifying and comprehensive approach, we in particular utilize this procedure to characterize time-reversal-symmetric crystalline topological insulating phases. Namely, the presented framework can be employed to quantify and elucidate topological invariants that are stable with regard to the addition of extra bands, usually described in terms of K theories, as well as finer characterizations of band topology coined fragile topology. Our setup allows us to naturally lift spinless notions to spinful ones, extending both homotopy and K theory. Amongst other things, we find that there exists an obstructed $\mathbb{Z}$-type classification protected by crystalline symmetries and TRS beyond the standard Fu-Kane-Mele $\mathbb{Z}_2$ classification. We have shown that this accounts for all nontrivial Wilson loop windings of a split elementary band representation (EBR). More importantly, this viewpoint can then be adopted to evaluate the proposed scheme of topological quantum chemistry [36,42,50] (TQC) by examining the EBR content. In particular, we have shown that while Wilson loop winding of split EBRs can unwind when embedded in higher-dimensional band spaces, two-band subspaces that remain separated by a band gap from the other bands conserve their Wilson loop winding, thus pointing to the fragile topology of split EBRs. This unifying perspective finds natural use in analyzing the origin of the fragile topology found in Ref. [51]. We then conclude with the observation that the stable Wilson loop winding, i.e., in the many-band limit, is only determined by the Fu-Kane-Mele $\mathbb{Z}_2$ invariant implying that further topological phases predicted in Ref. [43] must belong to the class of higher-order topological insulators (i.e., characterized through the nested Wilson loop) [52,53].

On the most general level, our work thus sets the basis of a systematic classification of topological crystalline phases with TRS by rigorously positioning three main classes: (1) unstable topologies that are only defined in few-band models and are rooted in homotopy classes of finite-dimensional Grassmannians, (2) stable topologies that persist upon the addition of an arbitrary amount of trivial bands and are described by K theories, (3) fragile topological phases bridging the two former classes and described within the formalism of vector bundle theory. It is expected that fragile topology leads to phase-sensitive observables [41,42,84] (e.g., Berry phase measurements) as opposed to the thermodynamical manifestations of stable topology (e.g., robust edge and surface states). Furthermore, our work has important implications for the characterization of obstructed atomic limits [50] which will be discussed elsewhere. The general applicability and effectiveness of our work is further underlined by potential impact on yet other recently discovered phases. Indeed, due to the similarity of codimension 1 and 2 defects [85–87], we anticipate that this approach can shed new light on the recently proposed higher-order topological insulators [52,53]. In fact, we already possess some insights on this subject, which we will report elsewhere. The above results should therefore be considered in the general context as an effective illustration of the versatility of the proposed framework.

Note added. Recently, we became aware of Ref. [88] that rigorously proves that for any one-band ground state with symmorphic magnetic space group G the vanishing of the first Chern class is equivalent to being a band representation. This is done through the analytical construction of a smooth,

periodic, and symmetric one-band section of the Bloch bundle. In our work we combine homotopy arguments and the numerical construction of multiband smooth, periodic, and rotation-symmetric Bloch frames (sections) with TRS in order to characterize the topology of a split EBR in class AII, leading to the complete classification of two-band subspaces in the layer groups L80 and L77. We furthermore discuss the effect of adding EBRs, thus revealing the fragile stability of the topology of split EBRs. We also became aware of Ref. [84] that appeared three months after our work and has some overlap with our work.

ACKNOWLEDGMENTS

We are grateful to A. Bernevig for stimulating discussions, and B. Bradlyn for bringing our attention to their Ref. [84], A. Alexandradinata and J. Höller for insightful comments about their works Refs. [41,88], and T. Bzdušek for a critical reading of an early version of the manuscript. A.B. and A.M.B.-S. acknowledge financial support from the Swedish Research Council (Vetenskapsrådet) Grant No. 621-2014-3721 and the Knut and Alice Wallenberg Foundation.

APPENDIX A: TWO-BAND SPINLESS TOPOLOGY

1. Tight-binding Hamiltonian and symmetries

We give here the generic structure of the spinless tight-binding Hamiltonian based on the layer group L77 with the point group C_{6v}. The Bloch basis is built from a complete set of localized Wannier functions through

$$|\varphi_A,\boldsymbol{k}\rangle = \frac{1}{\sqrt{N}}\sum_{\boldsymbol{R}_v} e^{i\boldsymbol{k}\cdot(\boldsymbol{R}_v+\boldsymbol{r}_A)}|w_A,\boldsymbol{R}_v\rangle,$$
$$|\varphi_B,\boldsymbol{k}\rangle = \frac{1}{\sqrt{N}}\sum_{\boldsymbol{R}_v} e^{i\boldsymbol{k}\cdot(\boldsymbol{R}_v+\boldsymbol{r}_B)}|w_B,\boldsymbol{R}_v\rangle, \tag{A1}$$

from which we obtain the tight-binding Hamiltonian in the sublattice site basis:

$$\mathcal{H} = \sum_{\boldsymbol{k}} \begin{pmatrix}|\varphi_A,\boldsymbol{k}\rangle\\ |\varphi_B,\boldsymbol{k}\rangle\end{pmatrix}^T \begin{pmatrix}h_{AA}(\boldsymbol{k}) & h_{AB}(\boldsymbol{k})\\ h_{BA}(\boldsymbol{k}) & h_{BB}(\boldsymbol{k})\end{pmatrix}\begin{pmatrix}\langle\varphi_A,\boldsymbol{k}|\\ \langle\varphi_B,\boldsymbol{k}|\end{pmatrix}. \tag{A2}$$

We define the symmetry-Bloch basis [34,40] through

$$\left(\left|\phi_{\Gamma_1},\boldsymbol{k}\right\rangle\left|\phi_{\Gamma_4},\boldsymbol{k}\right\rangle\right) = \left(|\varphi_A,\boldsymbol{k}\rangle\,|\varphi_B,\boldsymbol{k}\rangle\right)\hat{U}_S, \tag{A3}$$

with $\hat{U}_S = \frac{1}{\sqrt{2}}\left(\begin{smallmatrix}1 & 1\\ 1 & -1\end{smallmatrix}\right)$. We then have for the Hamiltonian written in the Bloch-symmetry basis

$$\mathcal{H} = \sum_{\boldsymbol{k}} |\boldsymbol{\phi},\boldsymbol{k}\rangle H_S(\boldsymbol{k})\langle\boldsymbol{\phi},\boldsymbol{k}|,$$
$$H_S(\boldsymbol{k}) = \begin{pmatrix}h_{11}^{(\Gamma_1)}(\boldsymbol{k}) & h_{14}^{(\Gamma_4)}(\boldsymbol{k})\\ h_{41}^{(\Gamma_4)}(\boldsymbol{k}) & h_{44}^{(\Gamma_1)}(\boldsymbol{k})\end{pmatrix}, \tag{A4}$$
$$|\boldsymbol{\phi},\boldsymbol{k}\rangle = \left(\left|\phi_{\Gamma_1},\boldsymbol{k}\right\rangle\left|\phi_{\Gamma_4},\boldsymbol{k}\right\rangle\right),$$

where the superscript of matrix element $h_{\mu\nu}^{(\Gamma_j)}(\boldsymbol{k})$ marks that it behaves as a basis function of the IRREP Γ_j of C_{6v}.

Real-space crystal symmetries act on the symmetry-Bloch basis as

$$^{\{g|0\}}\left|\phi_{\Gamma_j},\boldsymbol{k}\right\rangle = \left|\phi_{\Gamma_j},g\boldsymbol{k}\right\rangle\chi^{(\Gamma_j)}(g), \tag{A5}$$

which leads to the following symmetry constraint of the Hamiltonian:

$$\hat{U}_g\cdot H_S(\boldsymbol{k})\cdot\hat{U}_g^\dagger = H_S(g\boldsymbol{k}), \tag{A6}$$

where

$$\hat{U}_g = \bigoplus_j \chi^{(\Gamma_j)}(g). \tag{A7}$$

Under a translation by a reciprocal lattice vector, the Bloch functions satisfy

$$\left|\phi_{\Gamma_j},\boldsymbol{k}+\boldsymbol{K}\right\rangle = \left|\phi_{\Gamma_j},\boldsymbol{k}\right\rangle\cdot\hat{T}(\boldsymbol{K}),$$
$$\hat{T}(\boldsymbol{K}) = \hat{U}_S^\dagger\cdot\begin{pmatrix}e^{i\boldsymbol{K}\cdot\boldsymbol{r}_A} & 0\\ 0 & e^{i\boldsymbol{K}\cdot\boldsymbol{r}_B}\end{pmatrix}\cdot\hat{U}_S,$$
$$H_S(\boldsymbol{k}) = \hat{T}(\boldsymbol{K})\cdot H_S(\boldsymbol{k}+\boldsymbol{K})\cdot\hat{T}^\dagger(\boldsymbol{K}). \tag{A8}$$

Spinless TRS takes a particularly simple form

$$H_S^*(\boldsymbol{k}) = H_S(-\boldsymbol{k}). \tag{A9}$$

We define the Bloch eigenstates through

$$|\boldsymbol{\psi},\boldsymbol{k}\rangle = |\boldsymbol{\phi},\boldsymbol{k}\rangle\cdot\breve{U}(\boldsymbol{k}),$$
$$|\psi_n,\boldsymbol{k}\rangle = |\boldsymbol{\phi},\boldsymbol{k}\rangle\cdot\breve{U}_n(\boldsymbol{k}), \tag{A10}$$

where $\breve{U}(\boldsymbol{k}) = (\breve{U}_1(\boldsymbol{k})\,\breve{U}_2(\boldsymbol{k}))$ is the matrix formed by the eigenvectors $\breve{U}_n(\boldsymbol{k})$ of $H_S(\boldsymbol{k})$. In the following, we write them as $[\breve{U}_n(\boldsymbol{k})] \equiv |u_n,\boldsymbol{k}\rangle$.

General symmetry properties of the Bloch eigenstates

The symmetry properties of the Bloch eigenstates can readily be derived from those of the symmetry-Bloch basis introduced above, i.e.,

$$^{\{g|0\}}|\psi_n,\boldsymbol{k}\rangle = |\psi_m,g\boldsymbol{k}\rangle\langle u_m,g\boldsymbol{k}|\hat{U}_g|u_n,\boldsymbol{k}\rangle. \tag{A11}$$

We define the periodic gauge for the eigenstates by the constraint

$$\left|u_n^p,\boldsymbol{k}+\boldsymbol{K}\right\rangle = \hat{T}^\dagger(\boldsymbol{K})\left|u_n^p,\boldsymbol{k}\right\rangle. \tag{A12}$$

It readily follows for a high-symmetry momentum point that contains g in its little cogroup [56], i.e., $g\bar{\boldsymbol{k}} = \bar{\boldsymbol{k}}+\boldsymbol{K}_g$,

$$^{\{g|0\}}\left|\psi_n^p,\bar{\boldsymbol{k}}\right\rangle = \left|\psi_m^p,\bar{\boldsymbol{k}}\right\rangle\left\langle u_m^p,\boldsymbol{k}\right|\hat{T}(\boldsymbol{K}_g)\hat{U}_g\left|u_n^p,\bar{\boldsymbol{k}}\right\rangle, \tag{A13}$$

and the elements of a matrix representation of g with the IRREP Γ_j of the space group is then given by

$$R^{\bar{\boldsymbol{k}}}_{\Gamma_j,mn} = \left\langle\psi_m^p(\Gamma_j),g\bar{\boldsymbol{k}}\right|^{\{g|0\}}\left|\psi_n^p(\Gamma_j),\bar{\boldsymbol{k}}\right\rangle$$
$$= \left\langle u_m^p(\Gamma_j),\bar{\boldsymbol{k}}\right|\hat{T}(\boldsymbol{K}_g)\hat{U}_g\left|u_n^p(\Gamma_j),\bar{\boldsymbol{k}}\right\rangle, \tag{A14}$$

where $|\psi_n^p(\Gamma_j),\bar{\boldsymbol{k}}\rangle$ is a basis function of the IRREP Γ_j of the little group at $\bar{\boldsymbol{k}}$. Also, the cell-periodic Bloch function transforms as

$$\left|u_n^p(\Gamma_j),g\bar{\boldsymbol{k}}\right\rangle = \hat{U}_g\left|u_m^p(\Gamma_j),\bar{\boldsymbol{k}}\right\rangle R^{\bar{\boldsymbol{k}}\dagger}_{\Gamma_j,mn}. \tag{A15}$$

2. Analytical ansatz of the occupied eigenstate

The tight-binding Hamiltonian written in the symmetry-Bloch basis can be expanded with Pauli matrices as

$$H_S(\boldsymbol{k}) = h_0^{(\Gamma_1)}(\boldsymbol{k})\hat{1} + h_z^{(\Gamma_1)}(\boldsymbol{k})\hat{\sigma}_z + h_y^{(\Gamma_4)}(\boldsymbol{k})\hat{\sigma}_y, \tag{A16}$$

with the component

$$\begin{aligned} h_0^{(\Gamma_1)}(\boldsymbol{k}) &= h_{AA}(\boldsymbol{k}) = h_{BB}(\boldsymbol{k}), \\ h_z^{(\Gamma_1)}(\boldsymbol{k}) &= \mathrm{Re}[h_{AB}(\boldsymbol{k})], \\ h_y^{(\Gamma_4)}(\boldsymbol{k}) &= -\mathrm{Im}[h_{AB}(\boldsymbol{k})]. \end{aligned} \tag{A17}$$

Crystalline symmetries impose $h_0^{(\Gamma_1)}(\boldsymbol{k})$ and $h_z^{(\Gamma_1)}(\boldsymbol{k})$ to be real and even under inversion, while $h_y^{(\Gamma_4)}(\boldsymbol{k})$ must be real and odd under inversion. It is a special feature of the two-band model, symmetric under the point group C_{6v}, that inversion symmetry ($\mathcal{I}$) and spinless TRS ($\mathcal{T} = \mathcal{K}$, $\mathcal{T}^2 = +1$) are also effectively satisfied, leading to the effective point group D_{6h} as the symmetry of the system (i.e., L80) and with the effective AZ class AI. In other words, whenever C_{6v} is assumed, the two-band model is too restrictive to allow inversion symmetry and TRS breaking terms. In the following, we drop the superscripts and write h_0, h_z, and h_y.

Thanks to the simplicity of the Hamiltonian, the eigenvalues and eigenvectors take a simple form

$$\begin{aligned} E_1(\boldsymbol{k}) &= h_0(\boldsymbol{k}) - \epsilon_0(\boldsymbol{k}), \\ E_2(\boldsymbol{k}) &= h_0(\boldsymbol{k}) + \epsilon_0(\boldsymbol{k}) \end{aligned} \tag{A18}$$

with $\epsilon_0(\boldsymbol{k}) = \sqrt{h_z(\boldsymbol{k})^2 + h_y(\boldsymbol{k})^2}$, and

$$|u_1, \boldsymbol{k}\rangle = \frac{1}{2}\begin{pmatrix} 1 - \frac{\epsilon_0(\boldsymbol{k})}{h_z(\boldsymbol{k}) - ih_y(\boldsymbol{k})} \\ -1 - \frac{\epsilon_0(\boldsymbol{k})}{h_z(\boldsymbol{k}) - ih_y(\boldsymbol{k})} \end{pmatrix}, \tag{A19}$$

$$|u_2, \boldsymbol{k}\rangle = \frac{1}{2}\begin{pmatrix} 1 + \frac{\epsilon_0(\boldsymbol{k})}{h_z(\boldsymbol{k}) - ih_y(\boldsymbol{k})} \\ -1 + \frac{\epsilon_0(\boldsymbol{k})}{h_z(\boldsymbol{k}) - ih_y(\boldsymbol{k})} \end{pmatrix}. \tag{A20}$$

It is important to note that in this form the wave function is single valued and smooth over almost all of the Brillouin zone. These properties are necessary conditions for the noncyclic Berry phase to be meaningful (see below in Appendix A 4). Hence, the above ansatz implicitly defines a smooth reference gauge. We discuss in Appendix A 5 the effect of small and large gauge transformations.

In the following, we distinguish between the occupied eigenstate with energy $E_1(\boldsymbol{k})$ and the unoccupied eigenstate with energy $E_2(\boldsymbol{k})$, and $E_1(\boldsymbol{k}) < E_2(\boldsymbol{k})$.

Since by symmetry $h_y(\Gamma) = 0$, the occupied eigenstate at Γ is

$$|u_1, \Gamma\rangle = \frac{1}{2}\begin{pmatrix} 1 + s_\Gamma \\ -1 + s_\Gamma \end{pmatrix}, \tag{A21}$$

with $s_\Gamma = -\mathrm{sign}\{h_z(\Gamma)\}$. At M_1 (see Fig. 1), it is

$$|u_1, M_1\rangle = \frac{1}{2}\begin{pmatrix} 1 - \frac{\epsilon_0(M_1)}{h_z(M_1) - ih_y(M_1)} \\ -1 - \frac{\epsilon_0(M_1)}{h_z(M_1) - ih_y(M_1)} \end{pmatrix}. \tag{A22}$$

By symmetry $h_y^{(\Gamma_4)}(g\boldsymbol{k}) = -h_y^{(\Gamma_4)}(\boldsymbol{k})$, therefore, the eigenvector at M_2 is

$$|u_1, M_2\rangle = |u_1, M_1\rangle^* = \frac{1}{2}\begin{pmatrix} 1 - \frac{\epsilon_0(M_1)}{h_z(M_1) + ih_y(M_1)} \\ -1 - \frac{\epsilon_0(M_1)}{h_z(M_1) + ih_y(M_1)} \end{pmatrix}. \tag{A23}$$

The energy eigenstate must also be an eigenstate of the symmetries of the system, therefore,

$$\begin{aligned} {}^{\{C_{2z}|0\}}|\psi_1, M_1\rangle &= |\psi_1, M_1\rangle\langle u_1, M_1|\hat{T}(-\boldsymbol{b}_1 - \boldsymbol{b}_2)\hat{U}_{C_{2z}}|u_1, M_1\rangle \\ &= |\psi_1, M_1\rangle \frac{h_z(M_1) - \sqrt{3}h_y(M_1)}{2\sqrt{h_z(M_1)^2 + h_y(M_1)^2}} \\ &\overset{!}{=} |\psi_1, \mathrm{M}_1\rangle s_\mathrm{M}, \end{aligned} \tag{A24}$$

where $s_M = \pm 1$ determines the IRREP at M. This leads to the equation

$$\frac{1 - \sqrt{3}t}{2\sqrt{1 + t^2}} = s_M \frac{\sqrt{h_z(M_1)^2}}{h_z(M_1)} \tag{A25}$$

with $t = h_y(M_1)/h_z(M_1)$. Since the left-hand side cannot be -1, we set $s_M = \mathrm{sign}\{h_z(M_1)\}$, and we are left with the equation

$$\frac{1 - \sqrt{3}t}{2\sqrt{1 + t^2}} = 1, \tag{A26}$$

from which we find $t = h_y(M_1)/h_z(M_1) = -\sqrt{3}$. Hence, we can rewrite the occupied eigenvector at M_1 as

$$|u_1, M_1\rangle = \frac{1}{2}\begin{pmatrix} 1 - \frac{2s_M}{1 + i\sqrt{3}} \\ -1 - \frac{2s_M}{1 + i\sqrt{3}} \end{pmatrix}. \tag{A27}$$

We readily have the C_{2z}-symmetry eigenvalues at Γ and M_1 of the occupied eigenstate are given by

$$\begin{aligned} \xi_2^\Gamma &= s_\Gamma = -\mathrm{sign}\{h_z(\Gamma)\}, \\ \xi_2^M &= s_M = \mathrm{sign}\{h_z(M_1)\}. \end{aligned} \tag{A28}$$

3. Real homotopy and topological invariant

Performing the change of basis corresponding to $(\sigma_y, \sigma_z) \to (\sigma_z, \sigma_x)$, the Hamiltonian becomes real. Terms with the third Pauli matrix must vanish as a consequence of the $C_2\mathcal{T}$ symmetry [indeed $C_2\mathcal{T}$ with $(C_2\mathcal{T})^2 = +1$ can be represented as the complex conjugation]. The classifying space of the two-band Hamiltonian is then $\mathrm{Gr}_1(\mathbb{R}^2) \cong \mathbb{RP}^1 \cong \mathbb{S}^1$ [63]. Therefore, $\pi_1(\mathrm{Gr}_1(\mathbb{R}^2)) = \pi_1(\mathbb{S}^1) = \mathbb{Z}$, i.e., the topology over any arbitrary one-dimensional base loop is captured by an integer topological invariant.

The topological invariant for $\pi_1(\mathrm{Gr}_1(\mathbb{R}^2)) = \mathbb{Z}$ can be computed as the winding number of the noncyclic Berry phase over a closed loop when the eigenvectors are defined in a gauge that is smooth almost everywhere and is periodic over the Brillouin zone (see also Appendix A 5 on the gauge invariance). Each nodal point of the band structure induces a vortex structure in the eigenvectors so that the winding of the noncyclic Berry phase captures the *vorticity* [63] of the nodal point. The above $\mathbb{Z}$ classification over base loops indicates that the vorticities of multiple nodal points are additive for the base loop that encircles them all.

While this local result is not affected by the presence of additional crystalline symmetries, we derive below that the hexagonal symmetries act as an obstruction on the winding of the noncyclic Berry phase. We do this by choosing a symmetric base loop that crosses high-symmetry points and encircles on half of the Brillouin zone, hence revealing the global topology of the crystalline spinless semimetal.

4. Symmetry-constrained noncyclic Berry phase

Below, we derive the consequences for the noncyclic Berry phase over a symmetric base loop that crosses high-symmetry points, hence revealing the global topology of the crystalline spinless semimetal.

An oriented base loop in momentum space can be parametrized as $l(t):[0,1]\to\mathbb{S}^1$, $t\mapsto l(t)$ ($l\cong\mathbb{S}^1$). Assuming that the occupied eigenstate $|u_1,\boldsymbol{k}\rangle$ is defined smoothly all along an oriented loop $l(t)$, the noncyclic Berry phase is defined as

$$\gamma[l(t)]=i\int_{l(t)}d\boldsymbol{k}(t)\cdot\boldsymbol{\mathcal{A}}(\boldsymbol{k}(t)), \tag{A29}$$

with the U(1) Berry connection $\mathcal{A}_\mu(\boldsymbol{k})=\langle u_1,\boldsymbol{k}|\partial_{k^\mu}u_1,\boldsymbol{k}\rangle$ with $\mu=x,y$.

The geometric phase factor of the occupied state over the closed loop l_β encircling K_1 (see Fig. 1) is then given by

$$e^{i\gamma[l_\beta]}=\left(e^{i\gamma[l'_\beta]}\right)^3, \tag{A30}$$

where the loop segment $l'_\beta=l_{M_1\Gamma}\circ l_{\Gamma M_2}$ is one third of the total loop, starting at M_2, crossing Γ, and ending at M_1 (see Fig. 1). Using the Wilson loop formalism [16,20,24,25,34,39,40], we write

$$e^{i\gamma[l'_\beta]}=\langle u_1,M_1|\hat{W}_{M_1M_2}|u_1,M_2\rangle \tag{A31}$$

with the Wilson loop operator $\hat{W}_{k_2k_1}=\prod_{\boldsymbol{k}}^{k_2\leftarrow k_1}|u_1(\boldsymbol{k})\rangle\langle u_1(\boldsymbol{k})|$. We now project the occupied eigenvector at every $\boldsymbol{k}$ on the eigenvector at Γ, i.e.,

$$|\tilde{u}_1,\boldsymbol{k}\rangle=|u_1,\boldsymbol{k}\rangle\langle u_1,\boldsymbol{k}|u_1,\Gamma\rangle \tag{A32}$$

(note that $|\langle u_1,\boldsymbol{k}|u_1,\Gamma\rangle|=1$), and rewrite

$$\begin{aligned}e^{i\gamma[l'_\beta]}&=\frac{\langle u_1,\Gamma|u_1,M_2\rangle}{\langle u_1,\Gamma|u_1,M_1\rangle}\,\langle\tilde{u}_1,M_1|\widetilde{\hat{W}}_{M_1M_2}|\tilde{u}_1,M_2\rangle\\&=\frac{\langle u_1,\Gamma|u_1,M_2\rangle}{\langle u_1,\Gamma|u_1,M_1\rangle}\,\exp\left\{-\int_{l'_\beta}d\boldsymbol{k}\cdot\widetilde{\boldsymbol{\mathcal{A}}}(\boldsymbol{k})\right\}.\end{aligned} \tag{A33}$$

Now, since $|\tilde{u}_1,\Gamma\rangle$ is real, after projecting the eigenvectors on it, we get the simplification $\widetilde{\boldsymbol{\mathcal{A}}}(\boldsymbol{k})=\langle\tilde{u}_1,\boldsymbol{k}|\partial_{\boldsymbol{k}}\tilde{u}_1,\boldsymbol{k}\rangle=\mathrm{Im}\,(\langle\tilde{u}_1,\boldsymbol{k}|\partial_{\boldsymbol{k}}\tilde{u}_1,\boldsymbol{k}\rangle)=0$. Therefore,

$$e^{i\gamma[l'_\beta]}=\frac{\langle u_1,\Gamma|u_1,M_2\rangle}{\langle u_1,\Gamma|u_1,M_1\rangle}. \tag{A34}$$

Substituting with the expressions of the eigenvectors derived above, we eventually find

$$e^{i\gamma[l'_\beta]}=\frac{2-(1+i\sqrt{3})\xi_2^\Gamma\xi_2^M}{2-(1-i\sqrt{3})\xi_2^\Gamma\xi_2^M}. \tag{A35}$$

5. Gauge dependence

Equation (4) of the main text is derived from Eq. (A35). Equation (A35) has been derived from the analytical expression of the occupied eigenstate (A21) that fixes the gauge [also Eq. (A21) is defined in terms of a set of Bloch basis functions (A1) that trivialize the total Bloch bundle [59]]. It is then relevant to ask whether the result (4) is invariant under a gauge transformation $|u_1(\boldsymbol{k})\rangle\to|u_1(\boldsymbol{k})\rangle e^{i\theta(\boldsymbol{k})}$, $\boldsymbol{k}\in l_\beta$, that leads to the change of the Berry phase $\gamma^{(0)}[l]\to\gamma^{(\theta)}[l]$. Such a gauge transformation can originate for instance from a different choice of trivialization of the total Bloch bundle, e.g., for distinct choices of gauge of the set of Bloch (Fourier) basis functions (A1) [59], or by using a different ansatz of the eigenstate (A21).

Keeping track of the gauge phase as we travel along the base loop l_β, which we parametrize as $t\in[0,1]\mapsto l(t)$ with $l(0)=l(1)$, the single valuedness of the wave function requires $\theta(\boldsymbol{k}(t))|_{t=1}=\theta(\boldsymbol{k}(t))|_{t=0}+n2\pi$. Let us decompose the gauge phase into the part that winds, θ_n, and the part that goes back to its original value after we run one time through the loop, i.e., $\theta(t)=\theta_0(t)+\theta_n(t)$ with $\theta_0(t=1)=\theta_0(t=0)$, $\theta_n(t=0)=0$, and $\theta_n(t=1)=2n\pi$. Then, the nonwinding part of the gauge $\theta_0(t)$ can be smoothly mapped to zero without changing the Berry phase, i.e., $\gamma^{(\theta_0)}[l]=\gamma^{(0)}[l]$. On the contrary, the winding part of the gauge θ_n defines a large gauge transformation that shifts the Berry phase as $\gamma^{(\theta_n)}[l]=\gamma^{(0)}[l]+n2\pi$. While large gauge transformations are allowed within equivalence classes defined up to bundle isomorphisms, they lead to distinct homotopy equivalence classes [58]. Therefore, Eq. (4) [obtained from Eq. (A35)] makes only sense under the assumption that large gauge transformations are excluded which is practically always possible by (i) always using the same reference trivialization of the total Bloch bundle [Eq. (A1)] [59], and (ii) using the same smooth reference gauge of the eigenstate [Eq. (A21)].

APPENDIX B: FOUR-BAND SPINFUL CASE WITH INVERSION SYMMETRY

Let us now consider the extension of tight-binding model (A2) when the spin degrees of the freedom are taken into account. The basis functions can then be taken as $(|\phi_{\Gamma_1},\sigma,\boldsymbol{k}\rangle,|\phi_{\Gamma_4},\sigma,\boldsymbol{k}\rangle)$ with $\sigma=\uparrow,\downarrow$. Assuming TRS and inversion symmetry ($\mathcal{I}$), there is no spin-flip (Rashba) SOC and we can split the four-band spinful Hamiltonian into spin-up and -down sectors as

$$\mathcal{H}_\sigma=\left(|\phi_{\Gamma_1,\sigma},\boldsymbol{k}\rangle\,|\phi_{\Gamma_4,\sigma},\boldsymbol{k}\rangle\right)H_{S,\sigma}(\boldsymbol{k})\begin{pmatrix}\langle\phi_{\Gamma_1,\sigma},\boldsymbol{k}|\\ \langle\phi_{\Gamma_4,\sigma},\boldsymbol{k}|\end{pmatrix}, \tag{B1}$$

where

$$\begin{aligned}H_\sigma(\boldsymbol{k})=h_0^{(\Gamma_1)}(\boldsymbol{k})\hat{1}+h_z^{(\Gamma_1)}(\boldsymbol{k})\hat{\sigma}_z+h_y^{(\Gamma_4)}(\boldsymbol{k})\hat{\sigma}_y\\+s_\sigma h_x^{(\Gamma_3)}(\boldsymbol{k})\hat{\sigma}_x\end{aligned} \tag{B2}$$

with $\sigma=\uparrow,\downarrow$ and $s_\uparrow=+1$, $s_\downarrow=-1$. The term $h_x^{(\Gamma_3)}(\boldsymbol{k})$ contains all the (non-Rashba) SOC terms. Comparing with the Hamiltonian written in the sublattice site basis, we have $h_x^{(\Gamma_3)}(\boldsymbol{k})=[h_{AA,\uparrow}(\boldsymbol{k})-h_{BB,\uparrow}(\boldsymbol{k})]/2$.

Each spin sector of the Hamiltonian $H_\sigma(\boldsymbol{k})$ closely resembles the two-band spinless Hamiltonian (A16). However, now the term $h_x^{(\Gamma_3)}$ effectively breaks spinless vertical mirror symmetries (the character for Γ_3 of vertical mirror symmetries are $\chi^{\Gamma_3}_{m_{x,y}} = -\chi^{\Gamma_4}_{m_{x,y}}$) and spinless TRS ($\mathcal{T} = \mathcal{K}$). Therefore, each spin block only effectively conserves the symmetries of the point group $C_{6h} \subset D_{6h}$, i.e., L80 (SG191)→ L75 (SG175), and belongs to the AZ class A (instead of AI). The classifying space of the four-band spinful inversion-symmetric model is then composed as

$$\mathcal{H}^{2+2}_{\mathrm{AII+L80}} = \mathcal{H}^{1+1}_{\mathrm{A+L75}} \oplus \mathcal{H}^{1+1}_{\mathrm{A+L75}}. \tag{B3}$$

Contrary to L77 (C_{6v}) and L80 (D_{6h}), L75 (C_{6h}) has no essential degeneracy at K and the spectrum of each spin-polarized subspace $\mathcal{H}^{1+1}_{\mathrm{A+L75}}$ can be gapped. Furthermore, since there is only a single orbital per site, the eigenstates of both spin sectors are either all even or all odd under mirror symmetry with respect to the basal plane σ_h. As a consequence, the spectrum of each spin subspace must be gapped since no symmetry-protected band crossing can be formed over the BZ. It is important to notice that for this reason, $H_{S,\sigma}$ as obtained above is not the most general Hamiltonian of the spinless two-band symmetry class A + L75. See the schematic example of a band structure in Fig. 2(b) where each band is labeled according to their IRREPs at every HSP and away for the HSPs (in this case, they are all odd under σ_h since we have assumed the orbital p_z at every site).

1. Analytical ansatz for the spin-polarized eigenstates

The eigenvalues and eigenstates of one spin-sector (B1) take again a simple form (we have dropped the superscripts for the components of the Hamiltonian)

$$\begin{aligned} E_{1,\sigma}(\boldsymbol{k}) &= h_0(\boldsymbol{k}) - \epsilon_0(\boldsymbol{k}), \\ E_{2,\sigma}(\boldsymbol{k}) &= h_0(\boldsymbol{k}) + \epsilon_0(\boldsymbol{k}), \end{aligned} \tag{B4}$$

where $\epsilon_0(\boldsymbol{k}) = \sqrt{h_x(\boldsymbol{k})^2 + h_y(\boldsymbol{k})^2 + h_z(\boldsymbol{k})^2}$, and

$$|u_1, \sigma, \boldsymbol{k}\rangle = \frac{1}{\sqrt{2}\mathcal{N}_1} \begin{pmatrix} 1 + \frac{s_\sigma h_x - \epsilon_0(\boldsymbol{k})}{h_z(\boldsymbol{k}) - i h_y(\boldsymbol{k})} \\ -1 + \frac{s_\sigma h_x - \epsilon_0(\boldsymbol{k})}{h_z(\boldsymbol{k}) - i h_y(\boldsymbol{k})} \end{pmatrix}, \tag{B5}$$

$$|u_2, \sigma, \boldsymbol{k}\rangle = \frac{1}{\sqrt{2}\mathcal{N}_2} \begin{pmatrix} 1 + \frac{s_\sigma h_x + \epsilon_0(\boldsymbol{k})}{h_z(\boldsymbol{k}) - i h_y(\boldsymbol{k})} \\ -1 + \frac{s_\sigma h_x + \epsilon_0(\boldsymbol{k})}{h_z(\boldsymbol{k}) - i h_y(\boldsymbol{k})} \end{pmatrix}, \tag{B6}$$

with the normalization factors $\mathcal{N}_i$ defined through the conditions $\langle u_i, \sigma, \boldsymbol{k} | u_i, \sigma, \boldsymbol{k}\rangle = 1$, $i = 1, 2$.

The above analytical ansatz of the occupied eigenstate, $|u_1, \sigma, \boldsymbol{k}\rangle$, can be used to derive the spin-polarized Chern number in a direct way. This is rather tedious though and we instead use an alternative algebraic approach below. We have checked numerically though that the direct computation of the Chern number with the above ansatz gives the same results as the algebraic results.

2. Derivation of Eq. (6)

We have argued in Sec. III that the Chern number is obtained from the flow of Berry phase as we sweep a base loop over the BZ. By symmetry it is enough to compute the contribution to the Chern number from the patch S_ρ that covers one sixth of the BZ (Fig. 1). This is given by $e^{i\gamma_\rho}$ ($\gamma_\rho \equiv \gamma[l_\rho]$). We here use the Wilson loop techniques [16,20,24,25,34,39–41] in order to derive the spin-polarized Berry phase (Chern number) algebraically.

We choose the occupied eigenstate as $|u_1, \boldsymbol{k}\rangle = |u_1, \uparrow, \boldsymbol{k}\rangle$ (see above). In the following derivation, we actually do not need the explicit expression of the eigenstate. We only need the eigenvalues of occupied eigenstate under the rotation C_{2z} at Γ and M_1, and under C_{3z} at Γ and K_1. In the following, we neglect the phase factor coming from the rotation of the spin and we use the character table of the single-valued IRREPs. We have argued that each spin-polarized sector can be seen as belonging to the symmetry class A + L75 with point group C_{6h}. The eigenvalues under C_{2z} and C_{3z} of the relevant IRREPs are then obtained from the compatibility relations from the IRREPs of D_{6h} to the IRREPs of C_{6h}; these are given in Table I.

Let us split the oriented boundary of S_ρ, l_ρ (see Fig. 1) into the successive segments that connect the HSPs $\{\Gamma, M_1, \Gamma', K_1\}$ ($\Gamma' = \Gamma + \boldsymbol{b}_1 + \boldsymbol{b}_2$), i.e., $l_\rho = l_d \circ l_c \circ l_b \circ l_a$, with $l_d = l_{\Gamma \leftarrow K_1}$, $l_c = l_{K_1 \leftarrow \Gamma'}$, $l_b = l_{\Gamma' \leftarrow M_1}$, and $l_a = l_{M_1 \leftarrow \Gamma}$. We further choose l_ρ such that $l_b = C_{2z}(l_a^{-1} - \boldsymbol{b}_1 - \boldsymbol{b}_2) \sim C_{2z} l_a^{-1}$ and $l_c = C_{3z}(l_d^{-1} - \boldsymbol{b}_2) \sim C_{3z} l_d^{-1}$, where $\sim$ means equal up to a translation by a reciprocal lattice vector. We then write the contribution to the Berry phase factor from the segment l_a as $e^{i\theta_a} = \langle u_1, M_1 | \hat{W}_a | u_1, \Gamma\rangle$ where $\hat{W}_a$ is the Wilson loop operator along the path l_a, i.e., $\hat{W}_a = \prod_{\boldsymbol{k}}^{l_a} |u_1, \boldsymbol{k}\rangle\langle u_1, \boldsymbol{k}|$, and similarly for the other segments l_b, l_c, l_d.

The Berry phase factor over the whole loop l_ρ is then given by

$$\begin{aligned} e^{i\gamma_\rho} &= e^{i\theta_d} \langle u_1, K_1 | \hat{W}_c | u_1, \Gamma'\rangle \langle u_1, \Gamma' | \hat{W}_b | u_1, M_1\rangle e^{i\theta_a} \\ &= e^{i\theta_d} \langle u_1, C_{3z}(K_1 - \boldsymbol{b}_2) | \hat{W}_c | u_1, C_{3z}(\Gamma - \boldsymbol{b}_2)\rangle \langle u_1, C_{2z}(\Gamma - \boldsymbol{b}_1 - \boldsymbol{b}_2) | \hat{W}_b | u_1, C_{2z}(M_1 - \boldsymbol{b}_1 - \boldsymbol{b}_2)\rangle e^{i\theta_a} \\ &= e^{i\theta_d} R_3^K \langle u_1, K_1 | \hat{T}(-\boldsymbol{b}_2) \hat{C}_{3z}^\dagger \hat{W}_c \hat{C}_{3z} \hat{T}^\dagger(-\boldsymbol{b}_2) | u_1, \Gamma\rangle \left(R_3^\Gamma\right)^\dagger R_2^\Gamma \langle u_1, \Gamma | \hat{T}(-\boldsymbol{b}_1 - \boldsymbol{b}_2) \hat{C}_{32z}^\dagger \hat{W}_b \hat{C}_{2z} \hat{T}^\dagger(-\boldsymbol{b}_1 - \boldsymbol{b}_2) | u_1, M_1\rangle \left(R_2^M\right)^\dagger e^{i\theta_a} \\ &= e^{i\theta_d} R_3^K \langle u_1, K_1 | \hat{W}_d^{-1} | u_1, \Gamma\rangle \left(R_3^\Gamma\right)^\dagger R_2^\Gamma \langle u_1, \Gamma | \hat{W}_a^{-1} | u_1, M_1\rangle \left(R_2^M\right)^\dagger e^{i\theta_a} \\ &= e^{i\theta_d} \left[\xi_3^K e^{-i\theta_d} \left(\xi_3^\Gamma\right)^{-1}\right] \left[\xi_2^\Gamma e^{-i\theta_a} \left(\xi_2^M\right)^{-1}\right] e^{i\theta_a} \\ &= \xi_3^K \xi_2^\Gamma \left(\xi_3^\Gamma \xi_2^M\right)^{-1}, \end{aligned} \tag{B7}$$

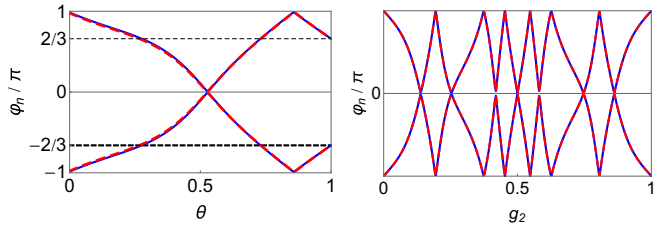

(a) $W[S_\rho] = +7\pi/3$ (b) $W_{II} = +7$

FIG. 11. Example of a split EBR with a Wilson loop winging of $W_{II} = +7$. (a) Flow of the Wilsonian phases over the patch S_ρ. (b) Flow of the Wilsonian phases over the BZ.

where we have used Eq. (A15) with the eigenvalues of the rotation symmetries (one-dimensional representations) at HSP $\bar{k}$ written as $\xi_2^{\bar{k}}$ for C_{2z} and $\xi_3^{\bar{k}}$ for C_{3z}, and where we have assumed the periodic gauge (A12). Now, taking into account all combinatorial ways of ordering the IRREPs of the effective spin-polarized EBR at the HSPs, one example is shown in Fig. 2(b), we eventually arrive at Eq. (6) in the main text.

3. Split EBR with Wilson loop winding of $W_{II} = +7$

We show in Fig. 11 a supplementary example of a four-band spinful topological phase with a Wilson loop winding of $W_{II} = +7$ in each two-band subspace. This phase was obtained for tight-binding parameters up to the 10th layer of neighbors. This indicates that arbitrary higher Wilson loop windings can be generated by increasing the range of the tight-binding parameters in analogy to topological insulators with high Chern numbers [89].

APPENDIX C: BLOCH EIGENSTATES OF THE SIX-BAND CASE AT Γ and K

After coupling the honeycomb lattice (with the split EBR $B_1^a + B_2^a$) to the triangular lattice (with the EBR $B_1^{a'}$), the doublets for the IRREPs $\overline{\Gamma}_9$ of the six-band model at Γ have the form

$$\left|\boldsymbol{\psi}^{B_1}_{\overline{\Gamma}_9}, \Gamma\right\rangle = \begin{bmatrix} \cos\vartheta\,|\phi_{\Gamma_1}, \uparrow, \Gamma\rangle + \sin\vartheta\,|\varphi_C, \uparrow, \Gamma\rangle \\ \cos\vartheta\,|\phi_{\Gamma_1}, \downarrow, \Gamma\rangle + \sin\vartheta\,|\varphi_C, \downarrow, \Gamma\rangle \end{bmatrix}^T,$$

$$\left|\boldsymbol{\psi}^{B_1'}_{\overline{\Gamma}_9}, \Gamma\right\rangle = \begin{bmatrix} \cos\vartheta\,|\varphi_C, \uparrow, \Gamma\rangle - \sin\vartheta\,|\phi_{\Gamma_1}, \uparrow, \Gamma\rangle \\ \cos\vartheta\,|\varphi_C, \downarrow, \Gamma\rangle - \sin\vartheta\,|\phi_{\Gamma_1}, \downarrow, \Gamma\rangle \end{bmatrix}^T, \quad \text{(C1)}$$

and the doublets for the IRREPs $\overline{K}_6$ at K have now the form

$$\left|\boldsymbol{\psi}^{B_1}_{\overline{K}_6}, K_1\right\rangle = \begin{bmatrix} \cos\bar{\vartheta}\,|\varphi_A, \uparrow, K_1\rangle + \omega\sin\bar{\vartheta}\,|\varphi_C, \downarrow, K_1\rangle \\ \cos\bar{\vartheta}\,|\varphi_B, \downarrow, K_1\rangle + \omega^*\sin\bar{\vartheta}\,|\varphi_C, \uparrow, K_1\rangle \end{bmatrix}^T,$$

$$\left|\boldsymbol{\psi}^{B_1'}_{\overline{K}_6}, K_1\right\rangle = \begin{bmatrix} \cos\bar{\vartheta}\,|\varphi_C, \downarrow, K_1\rangle - \omega^*\sin\bar{\vartheta}\,|\varphi_A, \uparrow, K_1\rangle \\ \cos\bar{\vartheta}\,|\varphi_C, \uparrow, K_1\rangle - \omega\sin\bar{\vartheta}\,|\varphi_B, \downarrow, K_1\rangle \end{bmatrix}^T, \quad \text{(C2)}$$

with $\omega = e^{i2\pi/3}$ and $\vartheta \in [0, \pi/2]$. These forms are readily obtained by inspection of the six-band Hamiltonian at Γ and K (we work with the most general tight-binding model allowed by symmetry including up to the 10th layer of neighbors). We have ordered the doublets such that the matrix representations of C_{3z}^+ are diagonal with the order $[e^{-i\pi/3}, e^{i\pi/3}]$ for $\overline{\Gamma}_9$ with the spin components ordered as $(\uparrow, \downarrow)$, and with $[e^{i\pi/3}, e^{-i\pi/3}]$ for $\overline{K}_6$ with the pseudospin components ordered as $(\tilde{\uparrow}, \tilde{\downarrow})$ for B_1 and as $(\tilde{\downarrow}, \tilde{\uparrow})$ for B_1'. The doublets at the inverted momentum $-K$ are then chosen such they are the conjugate partners under TRS, according to Eq. (10), with the doublets at K, i.e.,

$$\left|\boldsymbol{\psi}^{B_1}_{\overline{K}_6}, -K_1\right\rangle = \begin{bmatrix} \cos\bar{\vartheta}\,|\varphi_B, \uparrow, -K_1\rangle - \omega\sin\bar{\vartheta}\,|\varphi_C, \downarrow, -K_1\rangle \\ \cos\bar{\vartheta}\,|\varphi_A, \downarrow, -K_1\rangle - \omega^*\sin\bar{\vartheta}\,|\varphi_C, \uparrow, -K_1\rangle \end{bmatrix}^T,$$

$$\left|\boldsymbol{\psi}^{B_1'}_{\overline{K}_6}, -K_1\right\rangle = \begin{bmatrix} \cos\bar{\vartheta}\,|\varphi_C, \downarrow, -K_1\rangle + \omega^*\sin\bar{\vartheta}\,|\varphi_B, \uparrow, -K_1\rangle \\ \cos\bar{\vartheta}\,|\varphi_C, \uparrow, -K_1\rangle + \omega\sin\bar{\vartheta}\,|\varphi_A, \downarrow, -K_1\rangle \end{bmatrix}^T. \quad \text{(C3)}$$

A transformation of the Hamiltonian is here captured through the change of the only remaining free parameter ϑ. It is then straightforward to keep track of the effect at K of the coupling between the four bands $B_1 + B_2$ (from Wyckoff's position $2b$) with the extra B_1' (from Wyckoff's position $1a$). Starting with $\vartheta = 0$, the triangular lattice (C) is completely decoupled from the honeycomb lattice (A, B) and the $\overline{K}_6$ doublets both have a pure spin composition with the order $(\uparrow, \downarrow)$ in the basis that makes the matrix representation of C_{3z}^+ diagonal (see Sec. VI). Switching on the coupling between the two lattices, the doublets acquire the mixed spin structure of Eq. (C1). Then eventually at $\vartheta = \pi/2$, the two lattices are again completely decoupled and the doublets recover their pure spin composition but now in the reversed order $(\downarrow, \uparrow)$ while the ordering of the C_{3z}^+-symmetry eigenvalues is kept unchanged.

APPENDIX D: COMPLEMENTARY NUMERICAL SIX-BAND RESULTS

We show in Fig. 12 the six-band results analog to Fig. 8 in the main text but here generated from the other possible way of splitting the EBR of the honeycomb lattice, i.e., $B_1^a(2b) + B_2^a(2b)$.

In Fig. 13(a) we show the flow of Wilsonian phases over the BZ in the case where B_2^a is chosen as the two-band occupied subspace before the coupling with the extra bands B_1^a. This configuration is analog to Figs. 8(c) and 12(c) with a trivialized four-band unoccupied subspace [red line in Fig. 13(a)] and a two-band occupied subspace that remains topological with a Wilson loop winding of $W_{II} = \pm 4$ [blue dashed line in Fig. 13(a)].

In Fig. 13(b) we show the flow of Wilsonian phases over the BZ in the case where the EBR of the triangular lattice $B_1' = B_1^a(1a)$ has been chosen as the two-band occupied subspace before the coupling. In this case, the Wilson loops of the occupied and the unoccupied subspaces have both zero winding, indicating a fully trivial topology.

APPENDIX E: SMOOTH FRAME OF FOUR-BAND SUBSPACES

We give here a more detailed discussion of the stability of Wilson loop windings within a four-band subspace. Let us

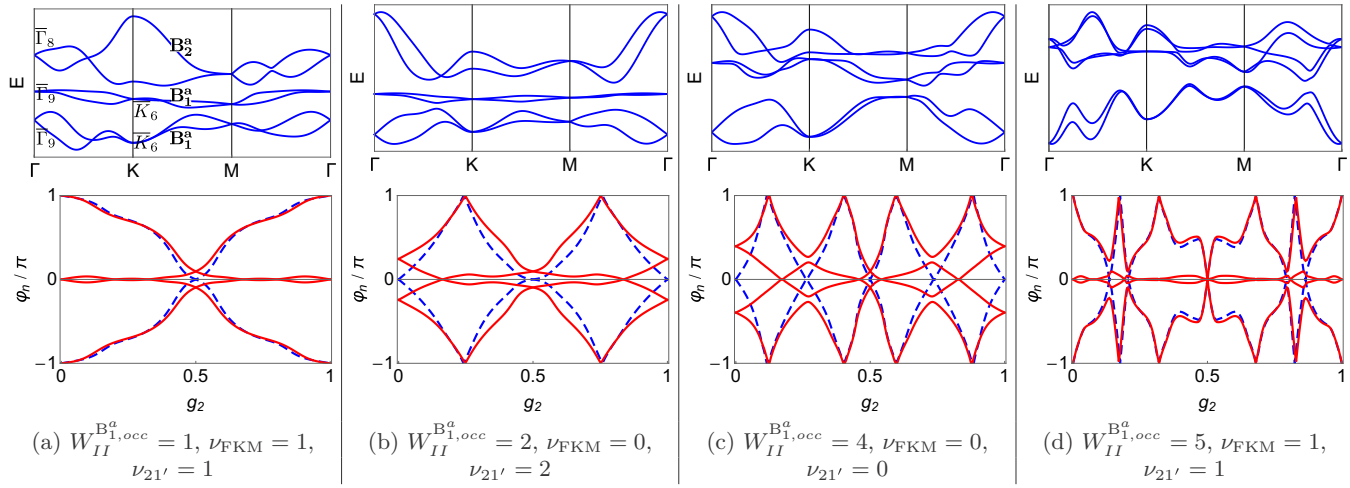

(a) $W_{II}^{B_{1,occ}^a} = 1$, $\nu_{\mathrm{FKM}} = 1$, $\nu_{21'} = 1$ (b) $W_{II}^{B_{1,occ}^a} = 2$, $\nu_{\mathrm{FKM}} = 0$, $\nu_{21'} = 2$ (c) $W_{II}^{B_{1,occ}^a} = 4$, $\nu_{\mathrm{FKM}} = 0$, $\nu_{21'} = 0$ (d) $W_{II}^{B_{1,occ}^a} = 5$, $\nu_{\mathrm{FKM}} = 1$, $\nu_{21'} = 1$

FIG. 12. Six-band topological phases obtained from the coupling of the split EBR $B_1^a + B_2^a$ with $B_1' = B_1^a$. The rest as for Fig. 8 of the main text.

assume, as it is the case in all our six-band numerical examples (given in Sec. VII and Appendix D), that after the coupling between the split EBR of the honeycomb lattice ($B_1 + B_2$) and the EBR of the triangular lattice (B_1'), a secondary band gap remains within the unoccupied subspace between $B_{2/1}$ and B_1'. We can then follow the procedure of Sec. VI in order to derive a smooth, periodic, and rotation-symmetric frame of each two-band BR composing the four-band subspace, i.e., taken separately. We have argued in Secs. VI and VIII B that such frame can always be found for a two-band subspace. Therefore, the Wilson loop winding of each two-band BR is quantized by symmetry and is classified by $W_{II} \in \{\pm\mathbf{1} + 3\mathbb{Z}, \mathbf{0}\}$ (Sec. VI). According to Sec. VIII B, the two-band Wilson loop winding of each two-band BR is unaffected by the coupling with other bands as long as the band gap separating each two-band BR from the other bands is preserved, i.e., as long as the coupling is adiabatic with respect to both the main band gap (between occupied and unoccupied subspaces) and the secondary band gap. Therefore, $W_{II}^{B_1'} = 0$ and $W_{II}^{B_{2/1}}$ keep the value it had before the coupling. If the two-band topology was stable, we would expect the Wilson loop winding of the four-band subspace $B_1' + B_{2/1}$ to be given by $W_{II}^{B_{2/1}} + W_{II}^{B_1'} = W_{II}^{B_{2/1}}$. We now argue that nothing guarantees *a priori* the stability of the two-band topology once it is imbedded in a four-band subspace.

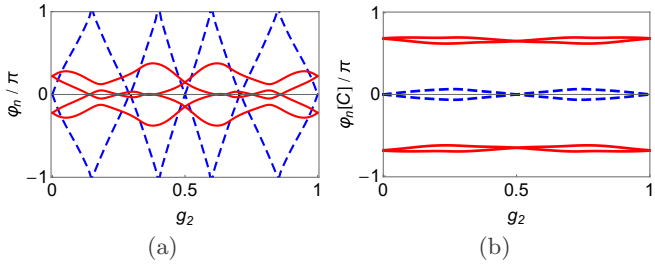

(a) (b)

FIG. 13. Similar to Fig. 12. (a) Wilson loops for $B_2 = B_2^a(2b)$ chosen as the two-band occupied subspace before coupling. (b) Wilson loops for $B_1' = B_1^a(1a)$ chosen as the two-band occupied subspace before coupling.

In the following, we need the orthogonality of the components of a Bloch frame. The smooth frame is obtained through a unitary transformation of the cell-periodic Bloch eigenstates at each $\boldsymbol{k}$, i.e., $|\boldsymbol{v}, \boldsymbol{k}\rangle = (|u_1, \boldsymbol{k}\rangle, |u_2, \boldsymbol{k}\rangle)^T \mathcal{U}(\boldsymbol{k})$ with $\mathcal{U}(\boldsymbol{k}) \in \mathrm{U}(2)$. Then, given the orthogonality of the Bloch eigenstates, $\langle u_2, \boldsymbol{k}|u_1, \boldsymbol{k}\rangle = 0$, the components of the smooth frame are also orthogonal, i.e., $\langle v_2, \boldsymbol{k}|v_1, \boldsymbol{k}\rangle = 0$, since the columns of $\mathcal{U}(\boldsymbol{k})$ form themselves an orthonormal basis of $\mathbb{C}^2$.

Let us write the separate smooth, periodic, and rotation-symmetric Bloch frames as $|\boldsymbol{v}^\nu, \boldsymbol{k}\rangle = (|v_1^\nu, \boldsymbol{k}\rangle, |v_2^\nu, \boldsymbol{k}\rangle)^T$ with $\nu = 1$ for $B_{2/1}$ and $\nu = 2$ for B_1' (see notations in Sec. VI). While each frame is orthogonal, they are not necessarily orthogonal to each other, i.e., $\langle v_i^\nu, \boldsymbol{k}|v_j^\nu, \boldsymbol{k}\rangle = \delta_{ij}$ but $\langle v_i^1, \boldsymbol{k}|v_j^2, \boldsymbol{k}\rangle \neq 0$. Therefore, the Wilson loop operator of the four-band subspace written in the separate smooth frames is given through $\widetilde{W}_{l_{\Gamma\mathrm{K}}} = \mathcal{P}^{11} + \mathcal{P}^{22} + \mathcal{P}^{12} + \mathcal{P}^{21}$ with the path-ordered products of projection operators $\mathcal{P}^{\nu\mu} = \prod_{\boldsymbol{k}}^{l_{\Gamma\mathrm{K}}} |\boldsymbol{v}^\nu, \boldsymbol{k}\rangle\langle \boldsymbol{v}^\mu, \boldsymbol{k}|$, i.e., the cross-product terms $\mathcal{P}^{12(21)}$ do not vanish. It then follows that the Wilson loop of the four-band subspace written in the separate smooth frames is in general not diagonal, i.e., $[\widetilde{\mathcal{W}}_{l_{\Gamma\mathrm{K}}}]_{ij}^{\nu\mu} = \langle v_i^\nu, \boldsymbol{k}|\widetilde{W}_{l_{\Gamma\mathrm{K}}}|v_j^\mu, \boldsymbol{k}\rangle \not\sim \delta_{\nu\mu}\delta_{ij}$. This prevents the symmetry-protected quantization of the Wilson loop spectrum. Indeed, the separate two-band smooth frames diagonalize the matrix representation of rotations at Γ and K but do not diagonalize the four-band Wilson loop. Conversely, if we compute the four-band smooth frame that diagonalizes the four-band Wilson loop, it is then not guaranteed to satisfy the rotation-symmetry constraint.

We have verified this numerically using the Soluyanov-Vanderbilt approach [76] and leave a formal proof for a future work. Therefore, we expect that in general the two-band subspace topology is unstable when it is imbedded within a four-band subspace.

[1] C. L. Kane and E. J. Mele, Phys. Rev. Lett. **95**, 226801 (2005).
[2] C. L. Kane and E. J. Mele, Phys. Rev. Lett. **95**, 146802 (2005).
[3] B. A. Bernevig, T. L. Hughes, and S.-C. Zhang, Science **314**, 1757 (2006).
[4] L. Fu, C. L. Kane, and E. J. Mele, Phys. Rev. Lett. **98**, 106803 (2007).
[5] X.-L. Qi and S.-C. Zhang, Rev. Mod. Phys. **83**, 1057 (2011).
[6] M. Z. Hasan and C. L. Kane, Rev. Mod. Phys. **82**, 3045 (2010).
[7] L. Fu and C. L. Kane, Phys. Rev. B **74**, 195312 (2006).
[8] L. Fu and C. L. Kane, Phys. Rev. B **76**, 045302 (2007).
[9] A. P. Schnyder, S. Ryu, A. Furusaki, and A. W. W. Ludwig, Phys. Rev. B **78**, 195125 (2008).
[10] Y. Ran, Y. Zhang, and A. Vishwanath, Nat. Phys. **5**, 298 (2009).
[11] R.-J. Slager, A. Mesaros, V. Juricic, and J. Zaanen, Phys. Rev. B **90**, 241403(R) (2014).
[12] J. C. Y. Teo and C. L. Kane, Phys. Rev. B **82**, 115120 (2010).
[13] A. Mesaros, R.-J. Slager, J. Zaanen, and V. Juricic, Nucl. Phys. B **867**, 977 (2013).
[14] R.-J. Slager, V. Juricic, V. Lahtinen, and J. Zaanen, Phys. Rev. B **93**, 245406 (2016).
[15] L. Fu, Phys. Rev. Lett. **106**, 106802 (2011).
[16] T. L. Hughes, E. Prodan, and B. A. Bernevig, Phys. Rev. B **83**, 245132 (2011).
[17] A. M. Turner, Y. Zhang, R. S. K. Mong, and A. Vishwanath, Phys. Rev. B **85**, 165120 (2012).
[18] R.-J. Slager, A. Mesaros, V. Juričić, and J. Zaanen, Nat. Phys. **9**, 98 (2012).
[19] V. Juričić, A. Mesaros, R.-J. Slager, and J. Zaanen, Phys. Rev. Lett. **108**, 106403 (2012).
[20] C. Fang, M. J. Gilbert, and B. A. Bernevig, Phys. Rev. B **86**, 115112 (2012).
[21] T. Morimoto and A. Furusaki, Phys. Rev. B **88**, 125129 (2013).
[22] K. Shiozaki and M. Sato, Phys. Rev. B **90**, 165114 (2014).
[23] C.-K. Chiu, J. C. Y. Teo, A. P. Schnyder, and S. Ryu, Rev. Mod. Phys. **88**, 035005 (2016).
[24] A. Alexandradinata, X. Dai, and B. A. Bernevig, Phys. Rev. B **89**, 155114 (2014).
[25] A. Alexandradinata, Z. Wang, and B. A. Bernevig, Phys. Rev. X **6**, 021008 (2016).
[26] A. Alexandradinata and B. A. Bernevig, Phys. Rev. B **93**, 205104 (2016).
[27] Z. Wang, A. Alexandradinata, R. J. Cava, and B. A. Bernevig, Nature (London) **532**, 189 (2016).
[28] H. Watanabe, H. C. Po, M. P. Zaletel, and A. Vishwanath, Phys. Rev. Lett. **117**, 096404 (2016).
[29] T. Bzdušek, Q. Wu, A. Rüegg, M. Sigrist, and A. A. Soluyanov, Nature (London) **538**, 75 (2016).
[30] L. Muechler, A. Alexandradinata, T. Neupert, and R. Car, Phys. Rev. X **6**, 041069 (2016).
[31] J. Kruthoff, J. de Boer, J. van Wezel, C. L. Kane, and R.-J. Slager, Phys. Rev. X **7**, 041069 (2017).
[32] K. Shiozaki, M. Sato, and K. Gomi, Phys. Rev. B **95**, 235425 (2017).
[33] A. Bouhon, R.-J. Slager, and T. Bzdušek, arXiv:1907.10611.
[34] A. Bouhon and A. M. Black-Schaffer, Phys. Rev. B **95**, 241101(R) (2017).
[35] H. C. Po, A. Vishwanath, and H. Watanabe, Nat. Commun. **8**, 50 (2017).
[36] B. Bradlyn, L. Elcoro, J. Cano, M. G. Vergniory, Z. Wang, C. Felser, M. I. Aroyo, and B. A. Bernevig, Nature (London) **547**, 298 (2017).
[37] R.-J. Slager, V. Juricic, and B. Roy, Phys. Rev. B **96**, 201401(R) (2017).
[38] R. M. Geilhufe, A. Bouhon, S. S. Borysov, and A. V. Balatsky, Phys. Rev. B **95**, 041103(R) (2017).
[39] R. Yu, X. L. Qi, A. Bernevig, Z. Fang, and X. Dai, Phys. Rev. B **84**, 075119 (2011).
[40] A. Bouhon and A. M. Black-Schaffer, arXiv:1710.04871.
[41] J. Höller and A. Alexandradinata, Phys. Rev. B **98**, 024310 (2018).
[42] J. Cano, B. Bradlyn, Z. Wang, L. Elcoro, M. G. Vergniory, C. Felser, M. I. Aroyo, and B. A. Bernevig, Phys. Rev. Lett. **120**, 266401 (2018).
[43] J. Kruthoff, J. de Boer, and J. van Wezel, Phys. Rev. B **100**, 075116 (2019).
[44] E. Khalaf, H. C. Po, A. Vishwanath, and H. Watanabe, Phys. Rev. X **8**, 031070 (2018).
[45] J. Zak, Phys. Rev. Lett. **45**, 1025 (1980).
[46] J. Zak, Phys. Rev. B **23**, 2824 (1981).
[47] L. Michel and J. Zak, Phys. Rev. B **59**, 5998 (1999).
[48] L. Michel and J. Zak, Europhys. Lett. **50**, 519 (2000).
[49] L. Michel and J. Zak, Phys. Rep. **341**, 377 (2001).
[50] J. Cano, B. Bradlyn, Z. Wang, L. Elcoro, M. G. Vergniory, C. Felser, M. I. Aroyo, and B. A. Bernevig, Phys. Rev. B **97**, 035139 (2018).
[51] H. C. Po, H. Watanabe, and A. Vishwanath, Phys. Rev. Lett. **121**, 126402 (2018).
[52] J. Langbehn, Y. Peng, L. Trifunovic, F. von Oppen, and P. W. Brouwer, Phys. Rev. Lett. **119**, 246401 (2017).
[53] W. A. Benalcazar, B. A. Bernevig, and T. L. Hughes, Phys. Rev. B **96**, 245115 (2017).
[54] International Tables for Crystallography, Volume A, Space-group symmetry, online edition (2006), edited by T. Hahn, https://it.iucr.org/Ab/.
[55] International Tables for Crystallography, Volume E, Subperiodic groups, online edition (2010), edited by V. Kopský and D. B. Litvin, https://it.iucr.org/E/.
[56] C. Bradley and A. Cracknell, *The Mathematical Theory of Symmetry in Solids* (Oxford University Press, Oxford, 1972).
[57] M. I. Aroyo, A. Kirov, C. Capillas, J. M. Perez-Mato, and H. Wondratschek, Acta Crystallogr., Sect. A **62**, 115 (2006).
[58] G. C. Thiang, Int. J. Geom. Methods Mod. Phys. **12**, 1550098 (2015).
[59] M. Fruchart, D. Carpentier, and K. Gawedzki, Europhys. Lett. **106**, 60002 (2014).
[60] B. A. Bernevig and T. L. Hughes, *Topological Insulators and Topological Superconductors* (Princeton University Press, Princeton, NJ, 2013).
[61] T. Bzdušek and M. Sigrist, Phys. Rev. B **96**, 155105 (2017).
[62] C. Fang, Y. Chen, H.-Y. Kee, and L. Fu, Phys. Rev. B **92**, 081201(R) (2015).
[63] X.-Q. Sun, S.-C. Zhang, and T. Bzdušek, Phys. Rev. Lett. **121**, 106402 (2018).
[64] E. Kiritsis, Commun. Math. Phys. **111**, 417 (1987).
[65] D. N. Sheng, Z. Y. Weng, L. Sheng, and F. D. M. Haldane, Phys. Rev. Lett. **97**, 036808 (2006).

[66] J. C. Y. Teo, L. Fu, and C. L. Kane, Phys. Rev. B **78**, 045426 (2008).
[67] E. Prodan, Phys. Rev. B **80**, 125327 (2009).
[68] J. Zak, Phys. Rev. B **20**, 2228 (1979).
[69] J. Zak, Phys. Rev. Lett. **62**, 2747 (1989).
[70] R. D. King-Smith and D. Vanderbilt, Phys. Rev. B **47**, 1651 (1993).
[71] D. Vanderbilt and R. D. King-Smith, Phys. Rev. B **48**, 4442 (1993).
[72] M. Taherinejad, K. F. Garrity, and D. Vanderbilt, Phys. Rev. B **89**, 115102 (2014).
[73] L. Elcoro, B. Bradlyn, Z. Wang, M. G. Vergniory, J. Cano, C. Felser, B. A. Bernevig, D. Orobengoa, G. de la Flor, and M. I. Aroyo, J. Appl. Crystallogr. **50**, 1457 (2017).
[74] R. Roy, Phys. Rev. B **79**, 195321 (2009).
[75] G. Panati, Ann. Henri Poincaré **8**, 995 (2007).
[76] A. A. Soluyanov and D. Vanderbilt, Phys. Rev. B **85**, 115415 (2012).
[77] A. Kitaev, *Periodic Table for Topological Insulators and Superconductors*, AIP Conf. Proc. No. 1134 (AIP, Melville, NY, 2009), p. 22.
[78] G. D. Nittis and K. Gomi, J. Geom. Phys. **86**, 303 (2014).
[79] G. De Nittis and K. Gomi, Commun. Math. Phys. **339**, 1 (2015).
[80] A. Hatcher, *Algebraic Topology* (Cambridge University Press, Cambridge, 2001).
[81] J. E. Moore, Y. Ran, and X.-G. Wen, Phys. Rev. Lett. **101**, 186805 (2008).
[82] D.-L. Deng, S.-T. Wang, C. Shen, and L.-M. Duan, Phys. Rev. B **88**, 201105(R) (2013).
[83] A. Hatcher, Vector Bundles and K-Theory (2003, unpublished), https://pi.math.cornell.edu/~hatcher/VBKT/VBpage.html.
[84] B. Bradlyn, Z. Wang, J. Cano, and B. A. Bernevig, Phys. Rev. B **99**, 045140 (2019).
[85] R.-J. Slager, L. Rademaker, J. Zaanen, and L. Balents, Phys. Rev. B **92**, 085126 (2015).
[86] R.-J. Slager, J. Phys. Chem. Solids **128**, 24 (2019).
[87] J.-W. Rhim, J. H. Bardarson, and R.-J. Slager, Phys. Rev. B **97**, 115143 (2018).
[88] A. Alexandradinata and J. Höller, Phys. Rev. B **98**, 184305 (2018).
[89] M. Udagawa and E. J. Bergholtz, J. Stat. Mech.: Theory Exp. (2014) P10012.
[90] V. Mathai and G. C. Thiang, J. Phys. A: Math. Theor. **50**, 11LT01 (2017).
[91] D. Kult, J. Åberg, and E. Sjöqvist, Phys. Rev. A **74**, 022106 (2006).
[92] M. S. Dresselhaus, G. Dresselhaus, and A. Jorio, *Group Theory* (Springer, Berlin, 2008).

Correction: The receipt history of this paper was reexamined and has been modified.